

CEBAF Program Advisory Committee Eight Cover Sheet

This proposal must be received by close of business on Thursday, April 14, 1994 at:

CEBAF

User Liaison Office, Mail Stop 12 B

12000 Jefferson Avenue

Newport News, VA 23606

Proposal Title

The Neutron Magnetic Form Factor from Precision Measurements
of the Ratio of Quasielastic Electron-Neutron to Electron-
Proton Scattering in Deuterium

Contact Person

Name: W. Brooks

Institution: CEBAF

Address: 12000 Jefferson Ave, Mail Stop 12 H

Address:

City, State ZIP/Country: Newport News, VA 23606

Phone: 804-249-7303

FAX:

E-Mail → Internet: BROOKSW@CEBAF.GOV

Experimental Hall: B

Total Days Requested for Approval: 15

Minimum and Maximum Beam Energies (GeV): 2.4, 4.0

Minimum and Maximum Beam Currents (μ Amps): --

CEBAF Use Only

Receipt Date: 4/14/94 18 94-017

By: L. Smith

HAZARD IDENTIFICATION CHECKLIST

CEBAF Experiment: _____

Date: _____

Check all items for which there is an anticipated need—do not check items that are part of the CEBAF standard experiment (HRSE, HRSH, CLAS, HMS, SOS in standard configurations).

Cryogenics <input type="checkbox"/> beamline magnets <input type="checkbox"/> analysis magnets <input type="checkbox"/> target <input type="checkbox"/> drift chambers <input type="checkbox"/> other	Electrical Equipment <input type="checkbox"/> cryo/electrical devices <input type="checkbox"/> capacitor banks <input type="checkbox"/> high voltage <input type="checkbox"/> exposed equipment	Radioactive/Hazardous Materials List any radioactive or hazardous/toxic materials planned for use: _____ _____
Pressure Vessels <u>5 mm</u> inside diameter <u>50 atm</u> operating pressure <u>Kapton</u> window material <u>minimal</u> window thickness	Flammable Gas or Liquids (incl. target) type: <u>H₂, D₂</u> flow rate: <u>0</u> capacity: <u>50 cm³</u>	Other Target Materials <input type="checkbox"/> Beryllium (Be) <input type="checkbox"/> Lithium (Li) <input type="checkbox"/> Mercury (Hg) <input type="checkbox"/> Lead (Pb) <input type="checkbox"/> Tungsten (W) <input type="checkbox"/> Uranium (U) <input type="checkbox"/> Other (list below) _____ _____
Vacuum Vessels <u>20 cm</u> inside diameter <u>vacuum to 4</u> operating pressure <u>Kapton</u> window material <u>minimal</u> window thickness	Radioactive Sources <input type="checkbox"/> permanent installation <input type="checkbox"/> temporary use type: _____ strength: _____	Large Mech. Structure/System <input type="checkbox"/> lifting devices <input type="checkbox"/> motion controllers <input type="checkbox"/> scaffolding or elevated platforms <input type="checkbox"/> other
Lasers type: _____ wattage: _____ class: _____ Installation <input type="checkbox"/> permanent <input type="checkbox"/> temporary Use <input type="checkbox"/> calibration <input type="checkbox"/> alignment	Hazardous Materials <input type="checkbox"/> cyanide plating materials <input type="checkbox"/> scintillation oil (from) <input type="checkbox"/> PCBs <input type="checkbox"/> methane <input type="checkbox"/> TMAE <input type="checkbox"/> TEA <input type="checkbox"/> photographic developers <input type="checkbox"/> other (list below) _____ _____ _____	Notes: <u>All above items will be</u> <u>part of a custom-built</u> <u>target for CLAS The</u> <u>target will be built</u> <u>at CEBAF</u> _____ _____

The Neutron Magnetic Form Factor from Precision Measurements of the Ratio of Quasielastic Electron-Neutron to Electron-Proton Scattering in Deuterium

W. K. Brooks, V. D. Burkert, D. Cords, B. A. Mecking, J. Mitchell, A. Yegneswaren
CEBAF

N. Bianchi, V. Muccifora, P. Rossi, E. De Sanctis
Istituto Nazionale di Fisica Nucleare, Frascati

P. Markowitz
University of Maryland

R. A. Miskimen
University of Massachusetts, Amherst

G. P. Gilfoyle, R. W. Major, and M. F. Vineyard
University of Richmond

CEBAF Large Acceptance Spectrometer Collaboration

Spokespersons: W. K. Brooks and M. F. Vineyard

Abstract

We propose to use the CEBAF Large Acceptance Spectrometer (CLAS) in Hall B to make precise measurements of the ratio of quasielastic electron-neutron to electron-proton scattering in deuterium over a Q^2 range from 0.3 to 5.1 (GeV/c)². The neutron magnetic form factor will be extracted from this ratio with the use of the more accurately determined proton form factors. The experiment will employ a dual target system that will allow the neutron detection efficiency of the CLAS electromagnetic calorimeters to be calibrated simultaneously with the quasielastic scattering measurements. We request 100 hours with an electron beam energy of 2.4 GeV, and 250 hours at 4 GeV. The results will provide severe tests of our understanding of nucleon structure.

1. Scientific Motivation

The structure of the proton and neutron is one of the most fundamental issues of nuclear physics. Elastic electron scattering provides detailed information about the electromagnetic structure of the nucleon. The differential cross section for elastic electron-nucleon scattering in the one-photon-exchange approximation is given by the Rosenbluth formula [1]:

$$\frac{d\sigma}{d\Omega} = \left(\frac{d\sigma}{d\Omega}\right)_{\text{Mott}} \left[\frac{G_E^2 + \tau G_M^2}{1 + \tau} + 2 \tau G_M^2 \tan^2\left(\frac{\theta}{2}\right) \right].$$

In this expression, $\left(\frac{d\sigma}{d\Omega}\right)_{\text{Mott}}$ is the Mott cross section, θ is the electron scattering angle, and $\tau = Q^2/4M^2$ where Q^2 is the square of the four-momentum transferred to the nucleon and M is the nucleon mass. The nucleon structure information is given by the Sachs electric and magnetic form factors G_E and G_M , respectively. These form factors provide a convenient meeting ground for the comparison between experiment and theoretical models of nucleon structure. In addition to being of fundamental importance in understanding nucleon structure, the form factors are a necessary input for calculations of nuclear response functions.

While differential cross sections for elastic electron-proton scattering have been measured [2] up to $Q^2 = 31 \text{ (GeV/c)}^2$, reliable separations of the two form factors have been made [3-6] only up to $Q^2 = 9 \text{ (GeV/c)}^2$. The results of these separations are shown in Fig. 1. The form factors are scaled by the dipole fit $G_D = (1 + Q^2/0.71)^{-2}$. The magnetic form factor is known with an accuracy of less than 3% over most of this Q^2 range. The uncertainties in G_{Ep} increase with Q^2 from about 3% to nearly 50%.

The neutron form factors have been measured [4,7-10] only up to $Q^2 = 4 \text{ (GeV/c)}^2$ and are shown in Fig. 2. These form factors have been determined with much less accuracy than the proton form factors. While some of the individual data points for G_{Mn} at $Q^2 < 2 \text{ (GeV/c)}^2$ have error bars of 5% or less, there are large fluctuations between different data sets which limits our

knowledge of G_{Mn} to about 20% in this Q^2 range. Only four points have been measured at $2 < Q^2 < 4 \text{ (GeV/c)}^2$. The present knowledge of G_{En} is also inadequate. The slope of G_{En} at $Q^2 = 0$ has been determined [11] with an accuracy of about 2% from the scattering of slow neutrons off atomic electrons. At higher Q^2 the errors are very large. The reason for the large uncertainties is due to the fact that the neutron form factors have to be determined from scattering off deuterium, and this will be discussed in the next section.

A variety of theoretical approaches have been used in attempts to describe nucleon form factors. The earliest efforts [12,13] focussed on the use of vector meson dominance (VMD) models. In this approach, the virtual photon interacts with the nucleon through vector mesons, and the nucleon form factors are expressed in terms of photon-meson coupling strengths and form factors describing the meson-nucleon vertices. These models have provided reasonable fits to the form factor data in the low Q^2 region. The results of one of these fits [13] is shown as the solid curves in Figs. 1 and 2. While the agreement with the data is reasonable at low Q^2 , discrepancies exist between the fit and the data for G_{Ep} and G_{Mn} at high Q^2 .

At $Q^2 > 10 \text{ (GeV/c)}^2$, the form factors have been calculated [14] in terms of dimensional scaling and perturbative quantum chromodynamics (PQCD). In this model, it is assumed that at large Q^2 the nucleons can be treated as bound systems of point-like quarks governed by the properties of the strong interaction. Dimensional scaling predicts that only the valence quarks are important, which are assumed to interact via a hard rescattering mechanism. These calculations predict that G_{Mp} scales asymptotically as Q^{-4} which is in good agreement with the data at high Q^2 .

A hybrid model has been developed by Gari and Krumpelmann [15] to predict the form factors at intermediate values of Q^2 . This model uses the VMD form at low Q^2 and constrains the high Q^2 results to agree with the PQCD calculations. The results of this approach are shown as the dashed curves in Figs. 1 and 2. These calculations are in reasonable agreement with much of the data at low Q^2 , and with the G_{Mp} data at high Q^2 . However, they do not reproduce most of the other data at high Q^2 .

Nesterenko and Radyushkin [16] have employed QCD sum rules based on quark-hadron duality to calculate the soft non-perturbative contribution to the nucleon form factors. They were able to describe cross section data in the intermediate Q^2 range with a calculation that included only the contribution from the lowest-order scattering diagram. The form factors calculated with this

model are shown as the dot-dashed curves in Figs. 1 and 2. The calculations are in fair agreement with the electric form factor data, and agreement with the magnetic form factors is approached at the highest Q^2 values where the calculation is expected to become valid.

Recently, two calculations [17,18] of nucleon form factors for $0 \leq Q^2 < 6 \text{ (GeV/c)}^2$ have been performed within the framework of relativistic constituent-quark models. The two models use different nucleon wave functions with the constituent-quark mass m and the confinement-scale parameter α as free parameters. Fits to the data result in $m \approx 0.25 \text{ GeV}$ and $\alpha \approx 0.6 \text{ GeV}$. The predictions of one of these models [17] are shown as the dotted curves in Figs. 1 and 2. Reasonable descriptions of the data are obtained at low Q^2 , however discrepancies between the theory and experiment are apparent in the high Q^2 range.

Another theoretical approach [19] treats the nucleons as being composed of quarks and diquarks. This model is a generalization of the hard scattering (PQCD) scheme discussed above and considers the diquarks as quasidelementary constituents which partly survive medium hard collisions. The diquarks can be considered as an effective description of correlations in the baryon wave function and provide a model for non-perturbative effects. This theoretical framework is constructed to predict the form factors at moderately large momentum transfer and is designed such that, when the diquarks dissolve into quarks at large momentum transfer, the hard scattering model emerges.

The techniques of quenched Monte Carlo lattice QCD has also been applied [20] to calculate electromagnetic form factors of the nucleon. A method was employed which characterizes one of the nucleon fields as a fixed zero-momentum secondary source. In the chiral limit, acceptable descriptions of the data were obtained for either dipole or monopole forms. The magnetic moment of the proton and neutron were extracted and found to be 10 to 15% low compared to experiment. In an extrapolation of the dipole fit of the form factors, the dipole-to-nucleon mass ratio was found to be about 7% lower than the experimental value. Also, positive values were obtained for the neutron electric form factor.

While all of the theoretical models described above agree with some data over a limited Q^2 range, none of them describe all of the data. Although the proton form factors are fairly well determined, the present knowledge of the neutron form factors is inadequate to impose severe constraints on the models. We propose to use the CEBAF electron beam and the Large Acceptance Spectrometer (CLAS) in Hall B to make precise measurements of G_{Mn} over the Q^2 range from 0.3 to 5.1 (GeV/c)^2 . In addition to providing accurate information on the magnetic structure of the

neutron, these data will be important for the extraction of G_{En} from future measurements of polarization observables which determine a linear combination of G_{En} and G_{Mn} (see for example Refs. [21,22]).

2. The Experiment

2.1 Proposed Technique

The existing data on the magnetic form factor of the neutron have been extracted from measurements of quasielastic scattering off deuterium targets. Three methods have been used to extract G_{Mn} from the experimental information at higher Q^2

One method is to determine G_{Mn} from inclusive cross section measurements using a Rosenbluth separation. At low momentum transfer, the $D(e,e')$ cross section is dominated by the electric contribution which severely limits the accuracy with which the magnetic term can be determined. The contribution of the proton must be calculated and subtracted from the total magnetic contribution. This introduces significant uncertainties since two large numbers are subtracted to obtain a relatively small one. A theoretical uncertainty results from modeling the deuteron wave function and the inelastic background to the quasielastic cross sections. Also, final-state interactions must be taken into account.

The uncertainties caused by these effects are reduced significantly if exclusive measurements are made of the cross section ratio

$$R_D = \frac{\frac{d\sigma}{d\Omega}(D(e,e'n))}{\frac{d\sigma}{d\Omega}(D(e,e'p))}.$$

At the quasielastic peak and for higher Q^2 , this ratio is nearly equal to the ratio of the *free* electron-neutron to electron-proton cross sections. Therefore, this quantity can be expressed in terms of the electromagnetic form factors as

$$R_D \approx R_F = \frac{\left[\frac{G_{En}^2 + \tau G_{Mn}^2}{1 + \tau} + 2 \tau G_{Mn}^2 \tan^2\left(\frac{\theta}{2}\right) \right]}{\left[\frac{G_{Ep}^2 + \tau G_{Mp}^2}{1 + \tau} + 2 \tau G_{Mp}^2 \tan^2\left(\frac{\theta}{2}\right) \right]}.$$

The neutron form factors can be extracted from measurements of this ratio with the use of the more accurately determined proton form factors. The price that one pays for using this technique is that the neutron detection efficiency must be calibrated accurately.

Another technique is to perform quasi-coincidence $D(e,e'\bar{p})$ measurements in which scattering from the neutron is inferred by the absence of a proton in the direction of the transferred momentum. The $D(e,e'\bar{p})$ cross section is obtained by the subtraction of the measured $D(e,e'p)$ cross section from the measured inclusive cross section. This introduces systematic errors because, again, two large numbers are subtracted to obtain a small one. There are also uncertainties due to a lack of understanding and control of all processes that can lead to the absence of a proton, such as final-state interactions, multiple scattering, or proton reactions in absorbing materials. In addition, this method is again sensitive to the deuteron wave function.

The ratio method is generally considered the most model independent method for determining the neutron form factors. This technique has been employed in three previous experiments [4,10,23]. The results for R_D are shown in Fig. 3. Data for G_{Mn} have been extracted from these measurements at only six values of Q^2 between 0.093 and 1.53 (GeV/c)². These six points are expected to be the most reliable experimental values for G_{Mn} since they were obtained with the use of the ratio method. All other data for G_{Mn} were obtained with one of the other two methods, and the large systematic uncertainties associated with these techniques are likely to be responsible for the discrepancies between different data sets.

We propose to make precise measurements of the ratio R_D with the CLAS. The neutron magnetic form factor will be extracted from this ratio with the use of the more accurately determined proton form factors. We will employ the $e+p \rightarrow e'+n+\pi^+$ reaction to measure the neutron detection efficiency of the CLAS electromagnetic calorimeters simultaneously with the measurement of R_D . The use of this calibration reaction is described in detail in section 2.3. The resulting data will overlap the earlier measurements made with the ratio technique and extend them to $Q^2 = 5.1$ (GeV/c)².

2.2 Detector Acceptance for the Ratio Measurement

The detector acceptance for the quasielastic $D(e,e'n)$ reaction is shown as a function of Q^2 in Fig. 4 for electron bombarding energies of 2.4 and 4 GeV. In performing these simulations, we have assumed calorimeter coverage in the CLAS from 8 to 45° in six sectors with two large-angle modules extending the coverage to 75° in two opposite sectors. The distributions of accepted

events consist of three structures. The structures at low Q^2 correspond to neutron detection in the large-angle calorimeters. The high- Q^2 structures are due to electron detection in the large-angle calorimeters. The large structures in the centers of the distributions correspond to the detection of both the electron and the neutron in the forward calorimeters. The dips in-between the structures are the results of a small gap in the theta acceptance due to the space between the forward and large-angle calorimeters. The effect of this gap at a single beam energy would be to leave a significant hole in the Q^2 coverage of the measurement. This will be avoided by the use of two different beam energies such that the gap occurs for different and non-overlapping ranges in Q^2 . (There are additional advantages to this strategy; the Q^2 range covered is broader, and there is significant overlap of the measured data between the two energies. The latter fact provides a good test of systematic errors since the running conditions will be somewhat different at the two beam energies.)

The detector acceptance for the quasielastic $D(e,e'p)$ reaction is shown as a function of Q^2 in Fig. 5 for electron energies of 2.4 and 4 GeV. The accepted distributions are different from those of the $D(e,e'n)$ reaction since the proton acceptance is determined by the coverage of the drift chambers and the time-of-flight counters and does not depend upon the calorimeter coverage.

We plan to run with opposite magnetic field polarities at the two different energies. The data at 4 GeV will be taken with a polarity such that positively charged particles will bend away from the beam axis. The measurements at 2.4 GeV will be made with the opposite polarity such that negatively charged particles will be bent away from the axis. Although this requires a somewhat reduced luminosity, it will enable us to extend the low Q^2 limit of these measurements down to 0.3 (GeV/c)^2 and maximize the overlap with the earlier experiments using the ratio method.

In general, the strategy of this measurement with respect to acceptance is to limit the data to the (θ, ϕ) regions where there is full acceptance for both proton and neutron, and make identical cuts for each. Shown in Fig. 6 is the azimuthal angle ϕ_N versus the polar angle θ_N for nucleons recoiling from quasielastic scattering off deuterium for four Q^2 bins with a cut on the azimuthal angle of the scattered electron of $\pm 15^\circ$ about the midplane of the opposite sector. The electron beam energy used in these simulations is 4 GeV. The solid curves shown in the figure indicate the acceptance limit in this single sector of the CLAS. For quasielastic scattering the angular spread of the outgoing nucleons is determined essentially by the ratio of the deuteron Fermi momentum to the 3-momentum transferred to the nucleon. Thus, as the momentum transfer increases the angular

spread of the recoiling nucleons decreases. From Fig. 6 it is clear that we can use electron ϕ -acceptance cuts as large as 30° without the single-sector acceptance limit interfering with the recoil nucleon distribution. This means that the usable ϕ -acceptance is at least 50% for a broad range in theta.

2.3 Calibration Reaction

The primary experimental uncertainties in the determination of the ratio R_D are the neutron detection efficiency and the solid angle equivalence of the proton and neutron measurement. Both the detection efficiency and the angle information for the neutron may be obtained via a "calibration reaction" on a hydrogen target which is being bombarded by the beam simultaneously with the deuterium target. This reaction, $e+p \rightarrow e'+n+\pi^+$, will allow neutrons to be tagged by two charged particles over a range of kinematics which matches quasielastic scattering quite well. Additionally, the neutron angle is determined by reconstruction from the charged particle information and in this way the drift chamber geometry is related to the geometry of the electromagnetic calorimeter. This connection is otherwise primarily established through surveying measurements; it is important in that it ensures that the angle cuts on the neutron and proton are made within a consistent coordinate system. An additional calibration run with zero field may be useful in establishing the relationship between the drift chamber and electromagnetic calorimeter geometries for this experiment's dual target.

2.3.1 Target Design

We will develop a target for this experiment that will enable us to use the $e+p \rightarrow e'+n+\pi^+$ reaction to calibrate the neutron response of the calorimeters simultaneously with the measurements of quasielastic scattering from deuterium. This will assure that the calorimeters are calibrated with the same thresholds and background conditions at which the primary measurements of interest are made.

A conceptual design of the target is shown in Fig. 7. Two identical gas cells will be aligned along the beam axis such that the beam passes through one and then the other. One cell will contain hydrogen, the other deuterium. Six support ribs are shown surrounding the targets. The support ribs serve two functions; one is to maintain alignment with the vacuum beam pipe before and after the target without obscuring the active detector volume, and the other is to support the thin vacuum foils. With the two target cells separated by 3 cm, vertex reconstruction can be used to determine

from which cell an event originated. The hydrogen and deuterium gases will be alternated periodically between the two cells to average out any differences in acceptance for the two targets.

2.3.2 Neutron Detection Efficiency

In Fig. 8 the acceptance for the $e+p \rightarrow e'+n+\pi^+$ reaction is plotted for beam energies of 2.4 and 4.0 GeV as a function of Q^2 . It may be seen that for both beam energies there are generally two enhancements in the acceptance function. The one at lower Q^2 is primarily due to events in which both the electron and the neutron are detected in the forward calorimeter. This region will be referred to in the following as the “higher statistics case” since on average the count rate there will be higher. The smaller enhancement at larger Q^2 is primarily due to events where the electron is detected in the large angle calorimeters in two of the six sectors. This will be referred to as the “lower statistics case” since the count rate of calibration events will be lower.

In Fig. 9 the kinematics for neutrons tagged by detection of both e' and π^+ are plotted for a beam energy of 4.0 GeV. The pion momentum cutoff is 100 MeV/c (and additionally an angle-dependent cutoff for forward angles has been used). It may be seen that in the calibration reaction for a given neutron angle there is a range of accepted neutron momenta; this range extends almost up to the momentum of the quasielastically scattered neutrons. This continuum of tagged neutrons allows an extrapolation of detection efficiency in neutron momentum (for a given angle) which determines the efficiency of the detector for recoiling neutrons from quasielastic scattering. Two examples of this method are shown in Fig. 10. In Fig. 10a the data points are given by a GEANT simulation which includes the full geometry of the electromagnetic shower calorimeter with uniform scintillator attenuation lengths for a range of ϕ angles and a θ angle of 30 degrees. The error bars on the curve are the statistical errors from the simulation. While in detail the low energy cross sections in the GEANT/GHEISHA package may not be accurate at the few MeV level, this general behavior of the data is clearly to be expected. (Neutron detection in the time-of-flight counters is also an attractive prospect, but it has been neglected here for simplicity.) The curve through the points is an empirical function which is used next in performing the extrapolation. In Figs. 10b and 10c are plotted extrapolations of the neutron detection efficiency for typical lower and higher statistics cases for the requested beam time, for a 1 degree angular bin in theta. The count rates were estimated using the simulated detector acceptance and the $e+p \rightarrow e'+n+\pi^+$ cross sections calculated with the code AO of Burkert and Li [24]. The results of the AO calculation are presented in Fig. 11. This figure shows the total cross section (apart from the photon flux factor)

as a function of the center of mass total energy W ; the separate curves are for different values of Q^2 as indicated in the caption. It may be seen from this figure that the delta resonance dominates the neutron production for the calibration reaction at the lower values of Q^2 , while higher resonances are the primary contributors at higher Q^2 values.

The extrapolations shown in Fig. 10a and 10b (and associated error estimate) were performed by taking the empirical function in Fig. 10a, associating the errors obtained from the count rate estimates with the appropriate points on the empirical function, and then throwing this data according to its errors. The "new" data were then fitted to the empirical function and the extrapolation to the quasielastic momentum was performed. For the error estimate this procedure was repeated for a total of 10 trials, and the maximum spread of the extrapolated values was used as the estimate of the full range of the systematic error associated with the extrapolation. For the lower statistics case this was $\pm 1\%$, and this was taken as the neutron detection efficiency error for the data with lower acceptance (see Fig. 8). For the higher statistics case the extrapolation error was found by the above method to be $\pm 0.03\%$; this value is so small that other systematic errors become more important. A second systematic error which may be considered is the very small shift in the direction of the neutron due to the separated targets. This effect may be estimated geometrically by assuming a 10% response uniformity for the calorimeter, two 15 cm targets separated by 3 cm, a 10 cm stack width, and a typical scattering angle of 25 degrees. In this case the systematic error is approximately 0.4 %. Although this effect can be measured in principle by alternating the hydrogen and deuterium gas cells, it is likely that statistical errors will not allow much improvement over this number; therefore, 0.4% has been used as the estimate for the systematic error in the neutron detection efficiency for the higher acceptance data.

Fig. 12 illustrates the dependence of the detection efficiency on different energy deposit thresholds from the same GEANT calculation referenced above. Since the detection efficiency is measured simultaneously with the primary quasielastic reaction, all phototube gain and threshold drifts and rate sensitivities are integrated over in the calibration event. This obviates the need for explicit corrections for these effects; as a check the efficiency variation with time can be correlated with gain drifts as measured by the UV laser system.

For completeness the pion kinematics for the calibration reaction are shown in Fig. 13 for a beam energy of 4 GeV.

2.3.3 Neutron Angle Calibration

The neutron angle in the calibration events may be measured by reconstruction of the pion and electron tracks. The accuracy of this reconstruction is a function of the neutron momentum, with the highest accuracy being obtained for the higher momenta. This result is optimal for the present experiment since the kinematics of interest are at the highest neutron momenta. Because of the spatial separation between the hydrogen target and the deuterium target there is a small angle shift between the mean neutron angles from the two targets which ranges from 0.3 to 1.5 degrees across the calorimeter face.

The electromagnetic shower calorimeter, while primarily optimized for electron-pion discrimination, also functions quite well as a neutron detector with regard to both detection efficiency and angular resolution. In the calorimeter the hit position is read out in three views separated in angle by approximately 60 degrees. This gives redundant position information which allows the reconstruction of multiple hits. In the case of neutrons of 1 GeV/c or more, for a 20 MeV threshold a typical event is seen in all three views. The geometric area of overlap of scintillator stacks from three views forms a triangular "pixel", which enables reconstruction of the neutron angle. The precise determination of the impact point of the neutron is achieved by averaging energy-weighted hits in each view.

An excellent cross check on the angle measurements may be performed by plotting the neutron angle measured in the calibration reaction via charged particle tracking against the directly measured neutron angle calculated from the calorimeter information. This plot is given in Fig. 14 with the errors expected from statistics for the planned running time, using distribution widths predicted from the GEANT simulation and reconstruction errors for the charged particles due to multiple scattering and finite detector resolutions. Such a comparison will reveal any discrepancies between the nominal geometries of the two detectors and can form the basis for a correction method.

The geometry may also be checked with elastically scattered electrons from both of the target cells in a zero-field run which will provide a further consistency check between the drift chamber geometry and the calorimeter geometry. Zero-field and neutral-particle measurements take the fullest advantage of the calorimeter projective geometry.

2.4 Measurement Uncertainties

2.4.1 Introduction

In the measurement of the ratio R_D in the deuteron a number of experimental and theoretical

uncertainties are reduced or eliminated. For example, it is unnecessary to know the experimental luminosity, and radiative corrections are the same for both proton and neutron. Sensitivities to the deuteron wave function and uncertainties in final state interactions have been shown to be very small for quasielastic kinematics [25].

In addition to the above advantages to the general approach, in the proposed implementation of this method employing a calibration target simultaneously with the deuteron target there is a further advantage. A typical procedure in neutron detection is to measure detection efficiencies at a given point in time and then apply this measurement at a later time when the primary reaction is studied. The problem with this approach is that maintaining conditions of constant gain and threshold calibration requires very sensitive monitoring of these quantities over extended periods of time; this is possible, but requires much effort and has unavoidably some inherent error. In the present proposed scheme the sensitivities to gain and threshold stability normally inherent in neutron detection are removed since these affect the deuteron and the calibration data in an identical way.

Measurement of the solid angles of the nucleons is accomplished by ray tracing for the proton and by direct measurement in the electromagnetic shower calorimeter for the neutron. Because of the large acceptance of the spectrometer it is unnecessary to make edge corrections for the neutron response as is typically required for smaller detectors. It is possible in most of the kinematics to accept the entire cone of outgoing neutrons around the direction of the virtual photon with only minimal cuts to the wings of the distribution.

While the above considerations relate to the measurement of the ratio R_D , for the extraction of G_{M_n} in this method it is necessary to consider the present state of knowledge of the three other nucleon form factors as the last remaining significant source of uncertainty. In addition there are small theoretical uncertainties associated with obtaining the *free* nucleon ratio R_F from R_D . The ratio of the differential cross section for elastic scattering on free protons relative to free neutrons is given in section 2.1. In the proposed measurement the ratio measured is not for free nucleons but rather for nucleons bound in deuterium, which necessitates a correction factor $f=R_D/R_F$ which must be obtained from theoretical models of the deuteron. Joosse [10] has compared the calculations of two different theoretical models and concluded that at very low Q^2 this introduces an uncertainty of less than 2 % in the G_{M_n} measurement. Since the bulk of the correction is due to final-state interactions the magnitude of the correction is expected to decrease with increasing Q^2 .

2.4.2 Accuracy of the Neutron Detection Efficiency

The general method of obtaining the neutron detection efficiency with the calibration reaction has been outlined previously in section 2.3.2. This method is to measure tagged neutrons for a range of momenta at a given angle simultaneous with the quasielastic scattering measurement, and then to make an extrapolation from the momenta measured in the calibration data to the quasielastic momentum.

The behavior of the neutron detection efficiency as a function of momentum has been examined in GEANT. A typical set of curves was given in Fig. 12. These functions will be well-studied in both the present measurement and in other high-statistics runs in the CLAS. From systematic studies of the functional dependences of the neutron detection efficiency it is expected that a family of curves can be derived with few or no free parameters which may be employed in the extrapolation to quasielastic momenta. This extrapolation may then be performed on a pixel-by-pixel basis. Effects due to the small angle difference between the hydrogen and deuterium targets may be studied or compensated for by alternating between the two gases in each cell.

The errors due to the detection efficiency extrapolation and to the separation between the two targets have been studied as described in section 2.3.2. The errors used in the present estimate are as follows: for 2.4 GeV beam energy and $0.3 < Q^2 < 1.5 \text{ (GeV/c)}^2$, the assigned error is 0.4 % and for $1.65 < Q^2 < 2.35 \text{ (GeV/c)}^2$ the error is 1.0 %. For the 4.0 GeV beam energy, the error is 0.4 % for $0.8 < Q^2 < 4.0$ and for $4.0 < Q^2 < 5.3 \text{ (GeV/c)}^2$ the error is 1.0 %. These choices simply reflect the higher and lower acceptance categories for each energy as plotted in Fig. 8.

2.4.3 Solid Angle Ratio of Nucleons

The solid angles of the two detected nucleons are determined by different methods. The basic approach for both proton and neutron is to accept the cone of outgoing nucleons around the q vector calculated from the electron momentum and scattering angle. In general this outgoing cone is fully accepted by the detector. Cuts on the neutron and proton angle distribution introduce the potential for error if the angle calibrations are inaccurate; because these calibrations are in fact relatively accurate and the cuts are relatively wide, the overall error incurred is small. An example of a cross-check on the data is to calculate the ratio R_D for symmetric bands on either side of the peaks or for successively narrower cuts; for truly quasielastic scattering the ratio will be constant,

and away from the quasielastic condition the results can be compared to models. The error resulting from making these cuts is estimated in the following sections for the proton and for the neutron.

2.4.3.1 Absolute Accuracy of the Proton Angles

The absolute accuracy attainable for the proton angle measurement is limited by the track reconstruction in the drift chambers. While the initial calibrations will rely on surveying measurements, a number of long calibration runs are planned with the CLAS for zero-field measurements of elastically scattered electrons and other minimum ionizing particles. Within the multiple scattering limit of about 1 mr it is anticipated that the chamber-to-chamber alignment will be established to approximately the same accuracy. Opposite-sector checks will be possible with e-p elastic scattering on hydrogen to verify the angle-angle and angle-energy correlations, both in the zero-field runs and in the calibration reaction in this experiment. Beam monitors positioned upstream and near the target will measure the incident beam angle to a fraction of a mr. The accuracy in the ϕ angle is limited to approximately 2 mr. The presence of an extended target, any inoperative region 1 sections, and any residual drift nonlinearity within and outside of the magnetic field cause additional small complications. In any case the accuracy of the solid-angle ratio is limited by the neutron angle measurement, which is much poorer than for the proton, so the primary focus here is on the neutron angle measurement.

2.4.3.2 Absolute Accuracy of the Neutron Angles

Fig. 15 shows the distribution of neutron angles around the direction of the virtual photon for the quasielastic data and for background resonances. (Fig. 16 shows the same quantity with a cut on the single arm missing mass.) This distribution is shown for a Q^2 of 1.0 (GeV/c)²; for smaller Q^2 the distribution becomes broader and for larger Q^2 it narrows. Fig. 17 shows the error resulting from making cuts on these distributions using the known angular accuracy of the calorimeter reconstruction explained below. The momentum dependence of this quantity has been included in making this plot. The cross marks on each curve indicate the point of one standard deviation of the reconstructed angular distribution. It is seen that at lower values of Q^2 the cut may be placed at a wide range of locations to examine the behavior of the measured ratio as the data depart from quasielastic conditions. At higher Q^2 this is not feasible but as may be seen from this graph it is still possible to make a fairly narrow cut without incurring significant systematic error.

The geometry of the electromagnetic calorimeter relative to the opposite sector drift chamber may be established in the calibration event as well as through comparison of electron tracks through the drift chambers from elastic scattering to the electron position reconstruction in the calorimeter; zero-field runs also can establish this connection. It is desirable to use neutrons for this purpose since charged particles may have different reconstruction attributes in the projective geometry of the calorimeter and the pattern of energy deposition will be quite different. According to a simulation of the electron and pion trajectories in the calibration event, the neutron angle will be established by reconstruction of the electron and pion with a resolution of better than 0.7 degrees for 1 GeV/c neutrons, 0.3 degrees for 2 GeV/c neutrons, and to approximately 0.15 degrees for 3 GeV/c neutrons. The *direct* reconstruction error (in one particular reconstruction strategy of GEANT events) in the electromagnetic shower calorimeter is plotted as a function of neutron momentum in Fig. 18; a typical reconstruction of GEANT events is shown in Fig. 19. From these plots and the kinematic information for the quasielastic event it is seen that the angular resolution from the direct reconstruction is approximately 0.5 degrees. The calibration data binned in theta bins of one degree will yield a statistical error on these measurements of typically 0.5 - 2.0 %. Taking the absolute accuracy as one-fifth of a standard deviation as a prescription for both distributions (well justified by the high statistics) an estimate of 0.1 to 0.2 degrees per point for the absolute accuracy of this measurement is obtained. These errors are reduced if many points are used as in Fig. 14 to determine overall systematic angular biases between the calorimeter and drift chamber.

2.4.4 Present State of Knowledge of Nucleon Form Factors

While the measurement of the ratio R_D is independent of knowledge of the nucleon form factors, in order to extract G_{Mn} from this quantity it is necessary to have fairly precise knowledge of G_{Mp} and G_{Ep} , and in addition there is a small dependence on the value of G_{En} . In the following the current accuracy in the understanding of these form factors is presented, and the impact on the extraction of G_{Mn} is given.

The best known data of this kind in the Q^2 range of interest is for G_{Mp} . Recent measurements by Bosted et al. [6], Bartel et al. [4], Berger et al. [3], and Walker et al. [5] span the range 0.39 to 9 (GeV/c)².

In general the data from the first three measurements are compatible with each other, while the data of Walker et al. lies one standard deviation below the rest of the data. Except for the data

of Walker the errors over the range 0 - 4 (GeV/c)² are internally consistent and range from 3% down to less than 1%. Given the multiplicity of measurements and the uniform coverage it is possible to establish this form factor to about 1%. A plot of these data has been shown in Fig. 1.

The data for G_{Ep} from the same authors are also internally consistent with the exception of Walker et al. However, the errors are much larger than for G_{Mp} . Up to $Q^2 = 1$ (GeV/c)² the errors range from 2 to 4 % on the individual points of the best measurements. From $Q^2 = 1$ to 2 (GeV/c)² the errors range from 5 to 10 %. From $Q^2 = 2$ to 3 the only accurate measurement is one point by Bosted with a 6 % error, and from $Q^2 = 3$ to 4 the same group's measurements have errors of 10 and 12 %. Since an empirical function for this observable is fairly well known it is possible to obtain an estimate for its value which is somewhat better than the errors on the individually measured points.

In addition to the existing data, there is an approved proposal at CEBAF [26] to make a more accurate measurement of G_{Ep} . This data should be available before the analysis of the present experiment is complete. The errors for the approved part of the beam time range from 1.4 % at $Q^2 = 0.8$ (GeV/c)² to 3.5 % at $Q^2 = 3.5$ (GeV/c)². The errors assumed for this proposal are shown in Table 1; they rely in part on the data from this future experiment.

Table 1. Accuracy Assumed for G_{Ep} .

Q^2 (GeV)	Error on G_{Ep} (%)
0.0 - 1.0	1.7
1.0 - 2.0	3.0
2.0 - 3.0	3.0
3.0 - 4.0	4.0
4.0 - 5.0	10.0

2.4.5 Background Suppression

In the calibration event the neutron will be unambiguously identified by the missing mass reconstruction. A priori, this is not as clear in the deuteron data. Because the missing mass resolution is relatively good, the neutron will be fairly well separated from most of the two-pion background; however, for a precision measurement a high degree of background discrimination is required. A reconstruction which does not utilize the measured neutron kinematic variables will

suffer from broadening due to the Fermi motion in the deuteron, but the precision of the reconstruction does not change rapidly with Q^2 . Use of the measured angle and energy information for the neutron can be expected to give good results at lower neutron momenta but poorer results at higher momenta because of the finite timing resolution of the electromagnetic calorimeter for neutrons. The missing mass spectrum expected for quasielastic scattering has been simulated and is plotted in Figs. 20 and 21 for 2.4 GeV and in Figs. 22 and 23 for 4.0 GeV incident energy. The input to these simulations includes realistic cross sections for events of the form $e+N \rightarrow e' + X$, where X includes channels such as $\pi\Delta$ and neutron production through higher resonances. A high-mass tail from radiative effects on the neutron is expected to be a relatively small effect.

The missing mass is shown in Fig. 20 for a beam energy of 2.4 GeV and a Q^2 of 1.0 (GeV/c)². In this figure is plotted the “single-arm missing mass” (neutron kinematics not used) for the process $e+n \rightarrow e' + X$. It may be seen that the missing nucleon mass is fairly well separated from the pion processes. In Fig. 21 the same quantity is plotted with a 4 degree cut on the measured angle between the neutron and the virtual photon. Here it is seen that the background contribution to the peak with this cut is vanishingly small.

The same quantities are plotted for 4 GeV incident energy and a Q^2 of 4.0 (GeV/c)² in Figs. 22 and 23. For this beam energy the $n\text{-}\gamma$ angle cut is made at 2 degrees. Here the separation is no longer complete due to the action of one cut alone. Significant improvement can be obtained by additional constraints on the hadronic final states.

The time of flight spectrum for calorimeter events at a beam energy of 4 GeV is shown in Fig. 24. The photon peak is seen at 15 ns; in addition there is a broad peak combining the quasielastic peak centered at 18.5 ns and the resonance background centered at 19.5 ns. The estimated accidental rate is shown along the bottom of the plot as an almost negligibly small contribution. The small accidental rate is one of the great advantages of being able to run with low luminosity in a large acceptance spectrometer. For a rate of 10^6 hadrons per second and a 5 ns wide range of interest the expected accidental rate is 0.5 %.

2.4.6 Statistical Errors

The beam time request for this experiment is for 100 hours of 2.4 GeV beam at a total luminosity of $3 \times 10^{33} \text{ cm}^{-2} \text{ s}^{-1}$ and 250 hours of 4.0 GeV beam at a total luminosity of $10 \times 10^{33} \text{ cm}^{-2} \text{ s}^{-1}$. The expected count rates, cumulative number of events and resulting statistical errors (for

a particular binning scheme) for quasielastic scattering are given in Table 2 for the Q^2 bins indicated at a variety of Q^2 values. From this table it is clear that the experiment will be limited in accuracy by statistics at the higher Q^2 values and by systematic errors at the lower values of Q^2 .

Table 2. Rates and Statistical Errors for Quasielastic Scattering

Q^2 (GeV/c) ²	Q^2 Bin	Proton Rate (s ⁻¹)	Neutron Rate (s ⁻¹)	Proton Counts	Proton Error (%)	Neutron Counts	Neutron Error(%)
0.3	0.011	1.4	.085	515000	0.1	31000	0.6
0.5	0.020	1.2	0.14	433000	0.2	51000	0.4
1.1	0.043	0.36	0.074	328000	0.2	67000	0.4
1.5	0.059	0.14	0.034	130000	0.3	31000	0.6
2.3	0.090	0.15	0.042	137000	0.3	38000	0.5
2.7	0.11	0.089	0.025	80000	0.4	23000	0.7
3.5	0.14	0.030	0.089	27000	0.6	8000	1.1
4.3	0.17	0.004	0.001	3400	1.7	1000	3.1
5.1	0.20	0.001	0.0004	1000	3.1	300	5.6

2.4.7 Theoretical Corrections

While the basic experimental method proposed is not sensitive to the details of the deuteron wave function, there are still corrections which arise from using the deuteron as a target. The form factor for the free neutron is derived from the ratio of free neutron elastic scattering to free proton scattering R_F , which is in turn obtained from the ratio of quasielastic neutrons relative to quasielastic protons R_D . The adjustment factor relating the two quantities R_F and R_D is obtained from detailed theoretical models for the deuteron. The estimated size of the correction is plotted in Fig. 25. These estimates were obtained from a calculation by Arenhoevel [25] for kinematics spanning the range of this experiment by calculating the ratio R_D in the full model (including final state interactions, meson exchange currents, isobar configurations and relativistic corrections) and in the relativistically corrected plane-wave impulse approximation. The curves give the percentage difference between these two predictions for quasielastic kinematics in the upper line and integrated over one standard deviation in outgoing nucleon angle in the lower curve. Since a large phase space is accepted by the detector it will be possible to actually test the model as mentioned earlier

by measuring R_D as a function of deviation from quasielastic scattering. This will be particularly feasible at the lower values of Q^2 since the angle cuts can be made there over a wide range of angles without introducing significant error (ref. Fig. 17). As in earlier calculations of similar quantities by Arenhoevel and others [10] it is seen that there is little theoretical ambiguity in extracting the ratio R_F from R_D . Further theoretical guidance will be sought to obtain a variety of calculational support for this assertion, especially at the higher values of Q^2 . For this proposal the uncertainty has been assigned as half of the size of the correction factor since there is some model dependence in this quantity.

2.4.8 Summary of Systematic Errors

The effect of the systematic errors discussed in the previous sections on G_{Mn} is summarized for selected data points in Table 3. The systematic errors in the measurement of the ratio R_D are summarized in Table 4.

Table 3. Effect of systematic errors on G_{Mn} . All numbers are in units of percent error in G_{Mn} due to the error listed.

Q^2 (GeV/c) ²	Theoretical Correction	G_{Ep} Uncertainty	G_{Mp} Uncertainty	G_{En} Uncertainty	Solid Angle	Background Subtraction	Neutron Efficiency	Total
0.3	1.0	1.0	0.40	0.90	0.22	0.05	0.2	1.7
0.5	0.60	0.79	0.54	1.0	0.25	0.05	0.2	1.5
1.1	0.25	0.78	0.74	0.85	0.55	0.05	0.2	1.5
1.5	0.25	0.56	0.81	0.69	0.55	0.05	0.2	1.4
2.3	0.25	0.43	0.86	0.63	0.89	0.80	0.2	1.7
2.7	0.25	0.36	0.88	0.54	0.89	0.89	0.2	1.7
3.5	0.25	0.33	0.92	0.39	1.2	1.1	0.2	2.0
4.3	0.25	0.54	0.95	0.27	1.5	1.2	0.5	2.3
5.1	0.25	0.33	0.97	0.17	1.7	1.4	0.5	2.5

Table 4. Effect of systematic errors on the ratio R_D . All numbers are in units of percent error in R_D due to the error listed.

Q^2 (GeV/c) ²	Solid Angle	Background Subtraction	Neutron Efficiency	Total
0.3	0.45	0.1	0.4	0.61
0.5	0.50	0.1	0.4	0.64
1.1	1.1	0.1	0.4	1.2
1.5	1.1	0.1	0.4	1.2
2.3	1.8	1.6	0.4	2.4
2.7	1.8	1.8	0.4	2.6
3.5	2.4	2.2	0.4	3.3
4.3	3.0	2.4	1.0	4.0
5.1	3.5	2.8	1.0	4.6

3. Summary and Request

We propose to make precise measurements of the ratio of quasielastic electron-neutron to electron-proton scattering in deuterium over a Q^2 range from 0.3 to 5.1 (GeV/c)². The neutron magnetic form factor will be extracted from this ratio with the use of the more accurately determined proton form factors. The experiment will use the CLAS detector and a dual target system that will allow the neutron detection efficiency of the electromagnetic calorimeters to be calibrated simultaneously with the quasielastic scattering measurements. We request 100 hours with an electron beam energy of 2.4 GeV, and 250 hours at 4 GeV. The expected results from this experiment are compared to existing data in Figs. 26 and 27. As can be seen in the figures, the expected CLAS data offer a significant improvement in our experimental knowledge of G_{Mn} and will provide a severe test for nucleon structure models.

References

- [1] M. N. Rosenbluth, Phys. Rev. **79**, 615 (1950).
- [2] R. G. Arnold *et al.*, Phys. Rev. Lett. **57**, 174 (1986).
- [3] Ch. Berger *et al.*, Phys. Lett. **35B**, 87 (1971).
- [4] W. Bartel *et al.*, Nucl. Phys. **B58**, 429 (1973).
- [5] R. C. Walker *et al.*, Phys. Lett. **B224**, 353 (1989); **B240**, 522 (1990).
- [6] P. E. Bosted *et al.*, Phys. Rev. Lett. **68**, 3841 (1992).
- [7] A. S. Esauslov *et al.*, Yad. Fiz. **45**, 410 (1987) [Sov. J. Nucl. Phys. **45**, 258 (1987)].
- [8] R. G. Arnold *et al.*, Phys. Rev. Lett. **61**, 806 (1988).
- [9] A. Lung *et al.*, Phys. Rev. Lett. **70**, 718 (1993).
- [10] F. C. P. Joosse, Ph. D. thesis, 1993 (unpublished).
- [11] V. E. Krohn *et al.*, Phys. Rev. **148**, 1303 (1966).
- [12] F. Iachello, A. D. Jackson, and A. Linde, Phys. Lett. **43B**, 191 (1973).
- [13] G. Hohler *et al.*, Nucl. Phys. **B114**, 505 (1976).
- [14] G. P. Lepage and S. J. Brodsky, Phys. Rev. Lett. **43**, 545 (1979); **43**, 1625 (1979).
- [15] M. Gari and W. Krumpelmann, Z. Phys. **A322**, 689 (1985); Phys. Lett. **B173**, 10 (1986).
- [16] V. A. Nesterenko and A. V. Radyushkin, Phys. Lett. **128B**, 439 (1983).
- [17] P. L. Chung and F. Coester, Phys. Rev. **D44**, 229 (1991).
- [18] F. Schlumpf, SLAC-PUB-5968 (1992); SLAC-PUB-6050 (1993).
- [19] P. Kroll, M. Schurmann, and W. Schweiger, Z. Phys. **A338**, 339 (1991).
- [20] W. Wilcox, T. Draper, and K. F. Liu, Phys. Rev. **D46**, 1109 (1992).
- [21] D. Day (spokesperson), CEBAF E-93-026.
- [22] R. Madey (spokesperson), CEBAF E-93-038.
- [23] P. Stein *et al.*, Phys. Rev. Lett. **16**, 592 (1966).
- [24] V. Burkert and Z. Li, private communication.
- [25] H. Arenhovel, private communication.
- [26] C. F. Perdrisat (spokesperson) CEBAF E-93-027.

Figure Captions

Fig. 1. The electric and magnetic form factors of the proton as a function of Q^2 . The data are from references [3-6]. The curves are the results of theoretical calculations with the VMD model of Hohler *et al.* [13] (solid curves), the hybrid model of Gari and Krumpelmann [15] (dashed curves), the Nesterenko and Radyushkin QCD sum rule predictions [16] (dot-dashed curves), and the relativistic constituent-quark model of Chung and Coester [17] (dotted curves).

Fig. 2. The electric and magnetic form factors of the neutron as a function of Q^2 . The data are from Refs. [4,7-10]. The curves are the results of theoretical calculations with the VMD model of Hohler *et al.* [13] (solid curves), the hybrid model of Gari and Krumpelmann [15] (dashed curves), the Nesterenko and Radyushkin QCD sum rule predictions [16] (dot-dashed curves), and the relativistic constituent-quark model of Chung and Coester [17] (dotted curves).

Fig. 3. The ratio $R_D = \frac{d\sigma}{d\Omega}(D(e,e'n))/\frac{d\sigma}{d\Omega}(D(e,e'p))$ as a function of Q^2 . The data are from Bartel *et al.* [4] and Joosse [10].

Fig. 4. Generated and accepted Q^2 distributions simulated for the $D(e,e'n)p$ reaction at $E = 2.4$ and 4 GeV.

Fig. 5. Simulations showing generated and accepted Q^2 distributions for the $D(e,e'p)n$ reaction at $E = 2.4$ and 4 GeV.

Fig. 6. The azimuthal angle ϕ_N versus the polar angle θ_N for nucleons recoiling from quasielastic scattering off deuterium for four Q^2 bins with a cut on the azimuthal angle of the scattered electron of $\pm 15^\circ$ about the midplane of the opposite sector.

Fig. 7. Schematic drawings of the conceptual design of the target.

Fig. 8. Simulations showing generated and accepted Q^2 distributions for the $p(e,e'\pi^+n)$ reaction at $E = 2.4$ and 4 GeV.

Fig. 9. Momentum versus production angle for neutrons from the $e+p \rightarrow e'+n+\pi^+$ reaction at 4 GeV with the electron and π^+ accepted.

Fig. 10. Illustration of the method that will be used to extrapolate the neutron detection efficiency to the momentum of the neutrons from quasielastic scattering. (a) Detection efficiency versus neutron momentum given by a GEANT simulation (data points) which includes the full geometry of the electromagnetic shower calorimeter with uniform scintillator attenuation lengths for a range of ϕ angles and $\theta=30^\circ$. The curve is an empirical function used in performing the extrapolation. (b) Same as (a) except the errors on the data points reflect the statistics expected for a 1° angular bin in theta for the requested beam time at 2.4 GeV and the points have been randomly thrown according to these errors. (c) Same as (b) except at 4.0 GeV. (See text for more details.)

Fig. 11. Cross section as a function of invariant mass calculated with the code AO [24] for the $e+p \rightarrow e'+n+\pi^+$ reaction for $Q^2 = 0.1-5$ (GeV/c) 2 . The cross section decreases as Q^2 increases.

Fig. 12. Neutron detection efficiency versus momentum predicted by GEANT with uniform attenuation lengths for $\theta=30^\circ$ and a range of ϕ angles. The different curves are for different thresholds and number of views hit.

Fig. 13. Momentum versus production angle for positive pions from the $e+p \rightarrow e'+n+\pi^+$ reaction at 4 GeV with the electron and neutron accepted.

Fig. 14. Neutron angle determined via $e'-\pi^+$ reconstruction from the calibration reaction versus neutron angle determined directly from the calorimeter with realistic errors. This plot demonstrates the sensitivity of the method to the determination of systematic angle errors.

Fig. 15. Neutron angular distribution about the direction of the virtual photon for electron scattering angles between 25 and 30 degrees and a beam energy of 2.4 GeV. The distribution contains contributions from both quasielastic scattering and background processes. The width of

the distribution is due to the deuteron Fermi motion.

Fig. 16. Same as Fig. 15 except that a cut on missing mass has been applied to this distribution.

Fig. 17. Systematic error from neutron angle cuts on the broad neutron angle distribution. Data is shown for 7 values of Q^2 . The 1-standard-deviation points for each Q^2 value are indicated by cross-marks. This error is dominant in the determination of the neutron-proton solid angle ratio.

Fig. 18. Neutron angular resolution versus neutron momentum from the direct reconstruction from energy-weighted hits in multiple views in the electromagnetic shower calorimeter. This calculation was performed with GEANT using uniform attenuation lengths in the full detector geometry and a range in phi angles.

Fig. 19. GEANT simulation of the neutron theta-angle determination in the forward electromagnetic shower calorimeter. The data is for an event from the rear portion of the calorimeter with 2 GeV neutrons incident at a theta angle of 30 degrees and a range of phi angles. The event was reconstructed if at least 2 views were hit, and a 20 MeV energy deposit threshold was required.

Fig. 20. Missing mass spectrum for quasielastic scattering off deuterium with a Q^2 of 1.0 $(\text{GeV}/c)^2$ and an incident beam energy of 2.4 GeV.

Fig. 21. Same as Fig. 20 except that a 4 degree cut on the angle between the nucleon and the virtual photon has been applied.

Fig. 22. Same as Fig. 20 except at a beam energy of 4.0 GeV and a Q^2 of 4.0 $(\text{GeV}/c)^2$.

Fig. 23. Same as Fig. 22 except that a 2 degree cut on the angle between the nucleon and the virtual photon has been applied.

Fig. 24. Neutron timing spectrum at 4.0 GeV incident energy for a wide range of neutron angles. The leftmost peak is due to photons, the rightmost peak is due to quasielastically scattered neutrons

for $\Delta t < 19.5$ ns and to resonance production. The very small accidental rate is plotted as a flat background.

Fig. 25. Correction factor to be applied to R_D as a function of Q^2 to compensate for the effects of final-state interactions, meson-exchange currents, and isobar currents as calculated within the model of Arenhoevel [25].

Fig. 26. The ratio of e-n to e-p quasielastic scattering as a function of the square of the four-momentum transfer showing the accuracy which will be obtained in the current experiment compared to previous measurements. The errors are estimated as explained in the text.

Fig. 27. G_{Mn} as a function of the square of the four-momentum transfer showing the accuracy which will be obtained in the current experiment compared to previous measurements. The errors are estimated as explained in the text.

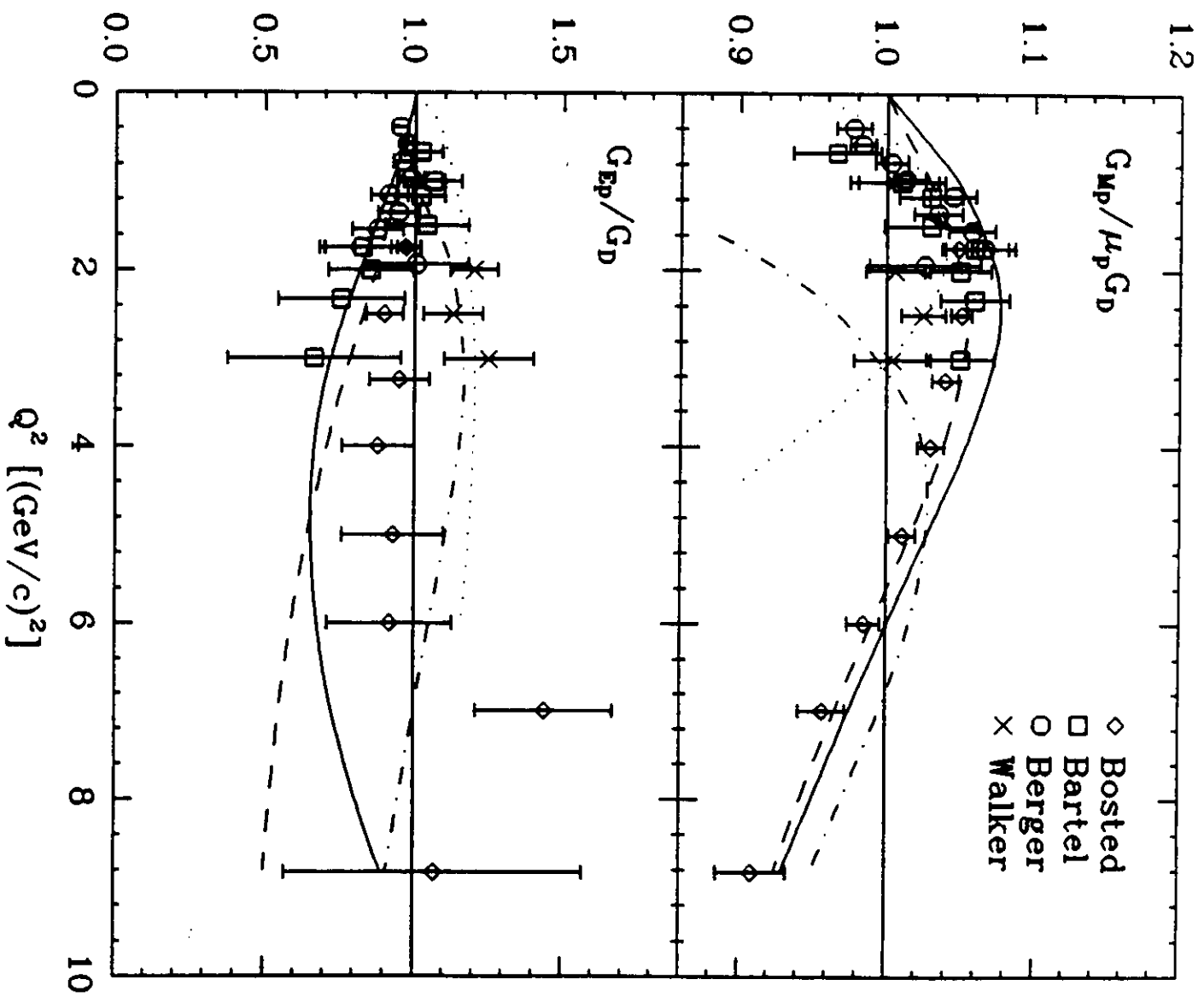


Fig. 1

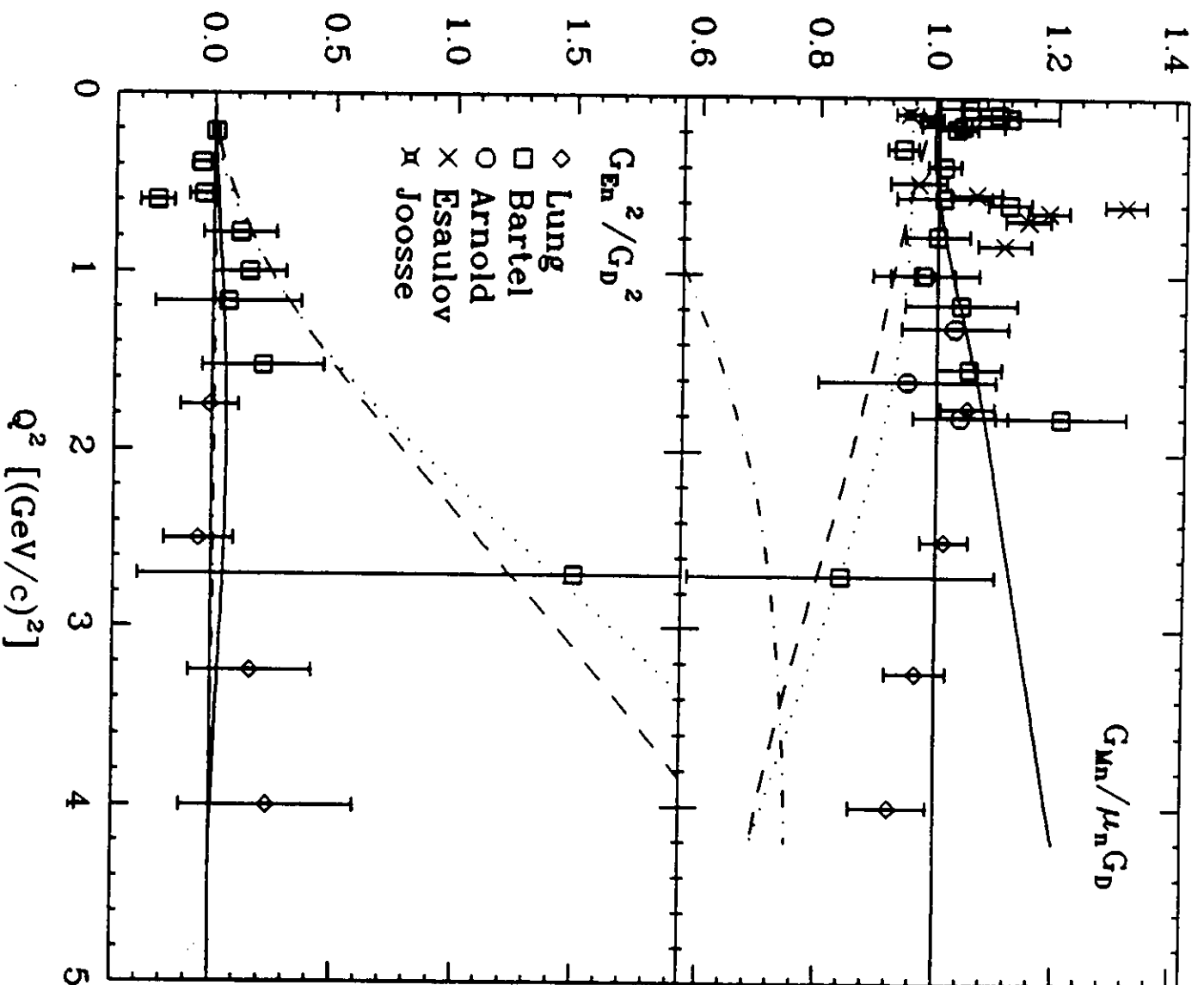


Fig. 2

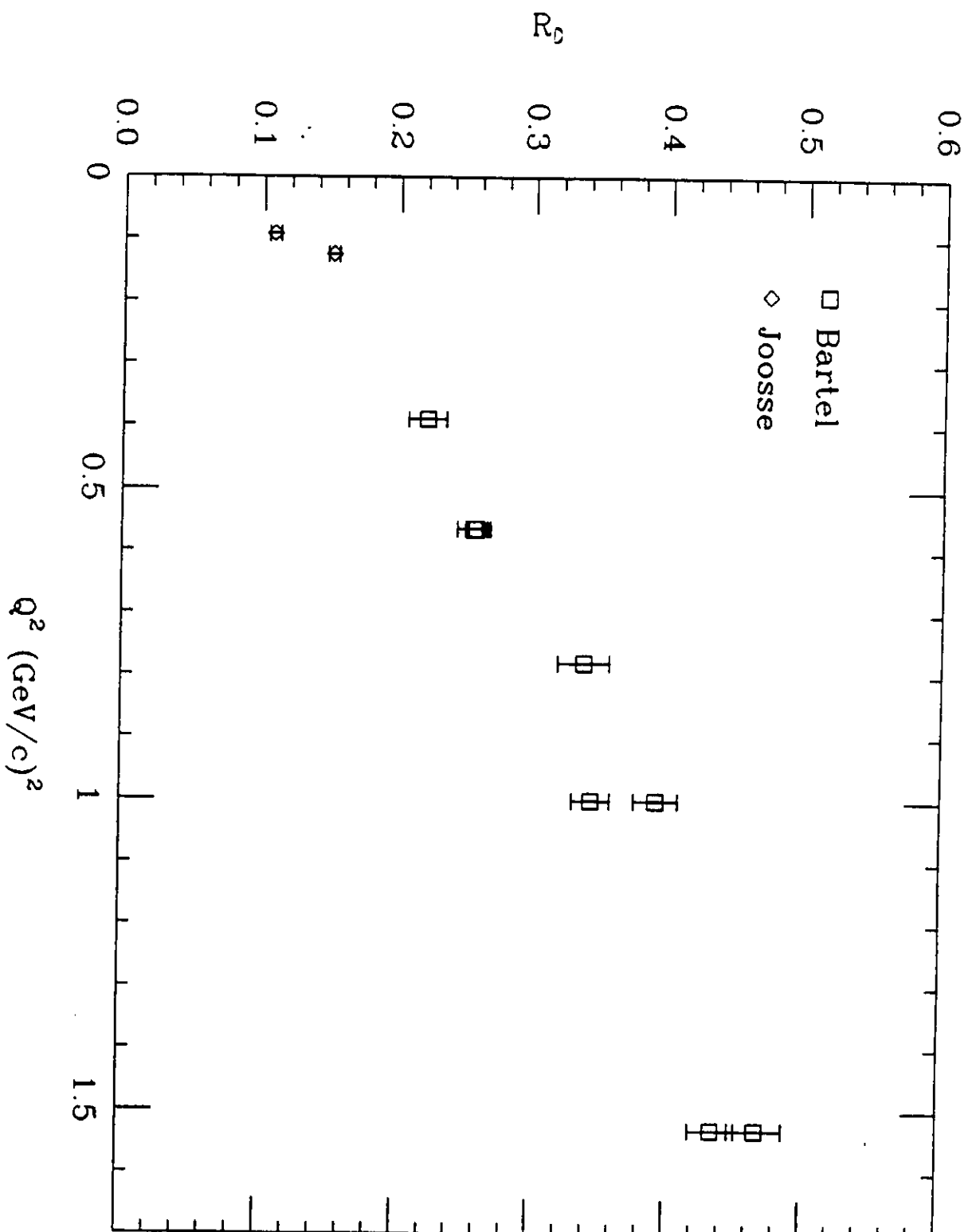


Fig. 3

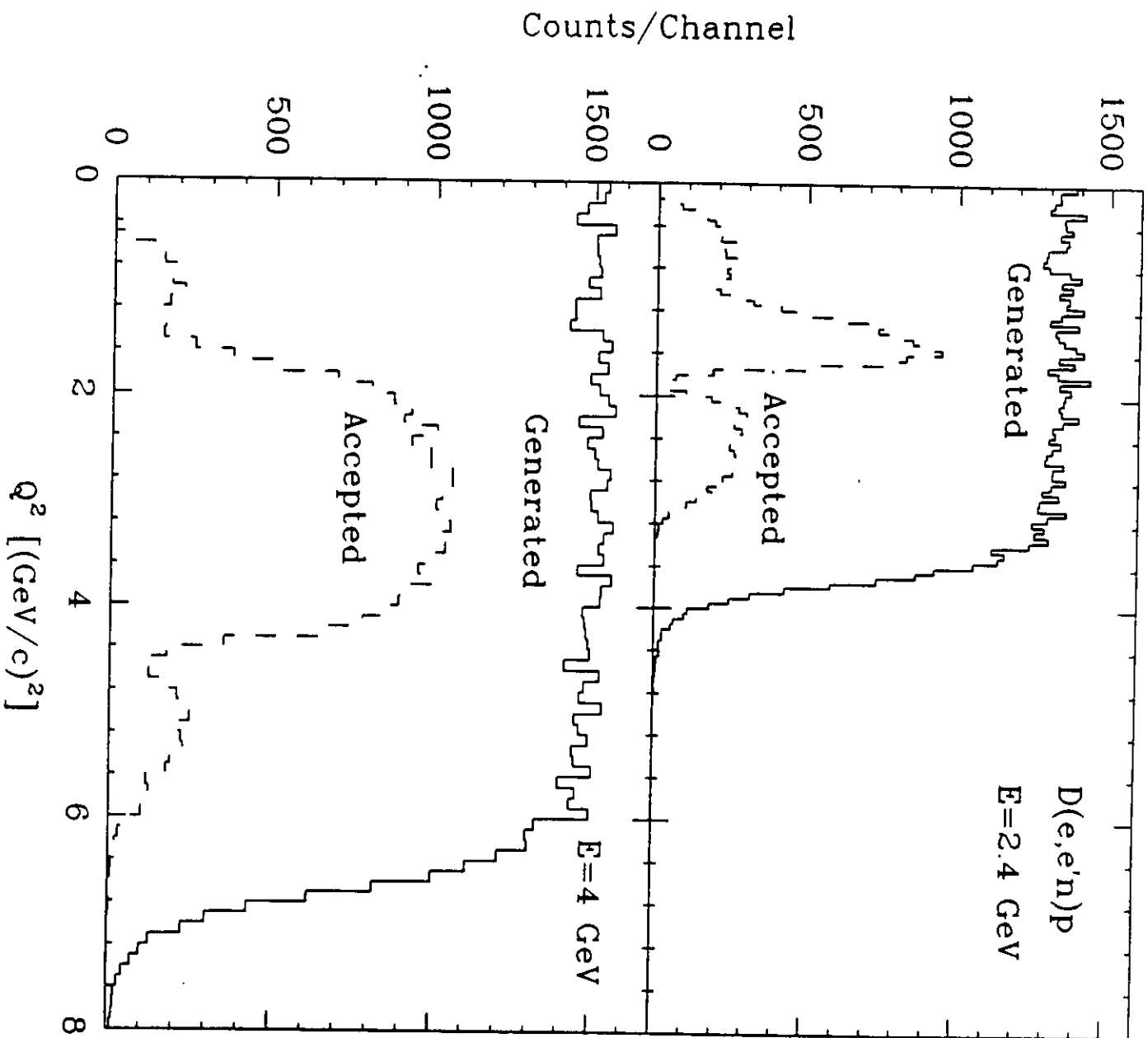


Fig. 4

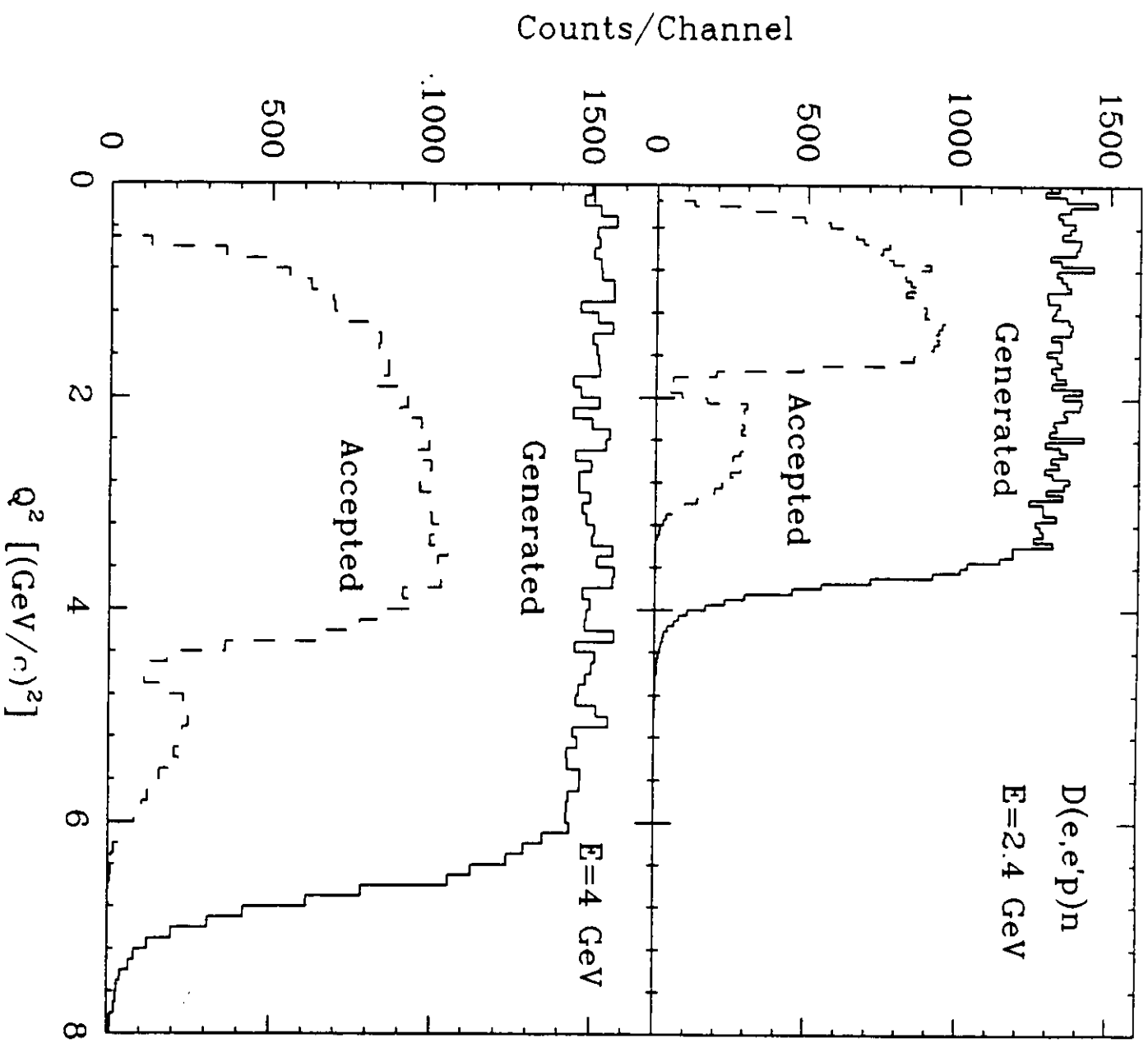


Fig. 5

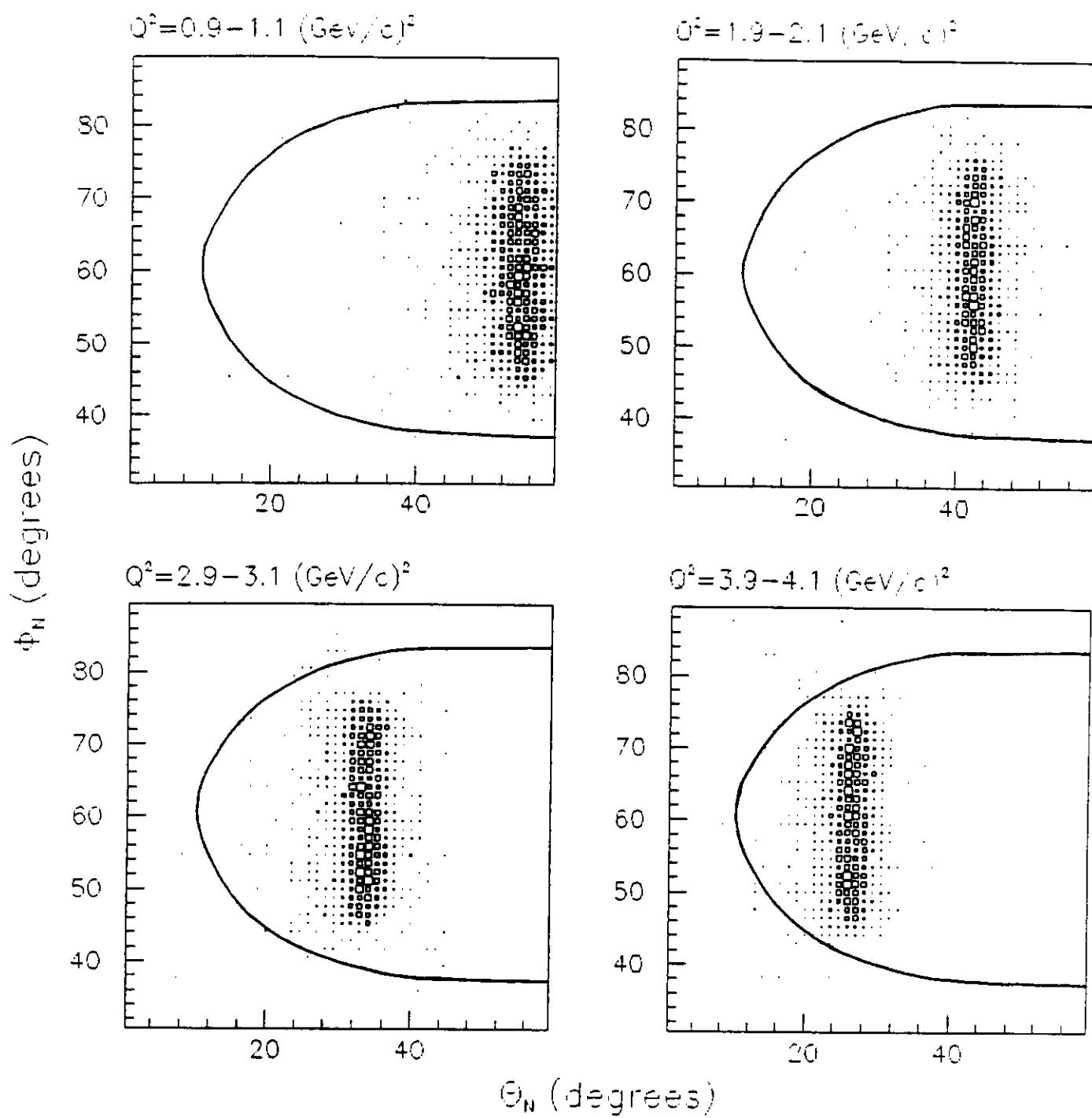


Fig. 6

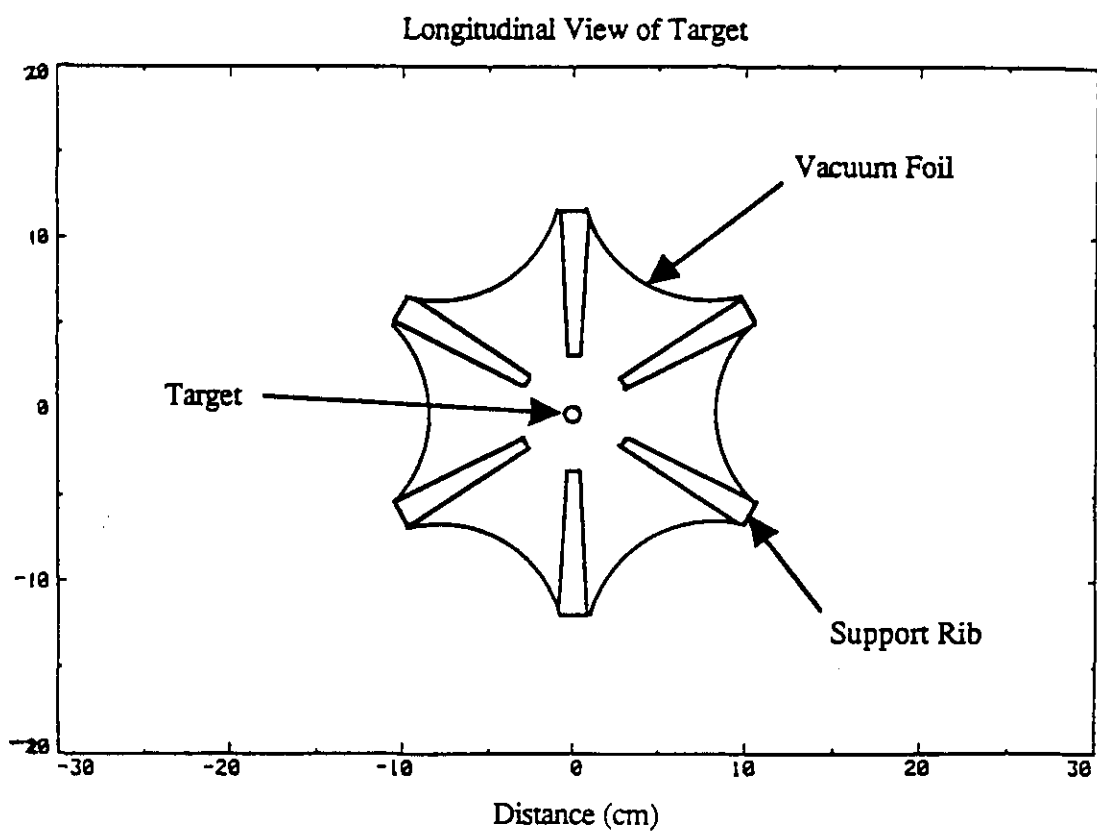
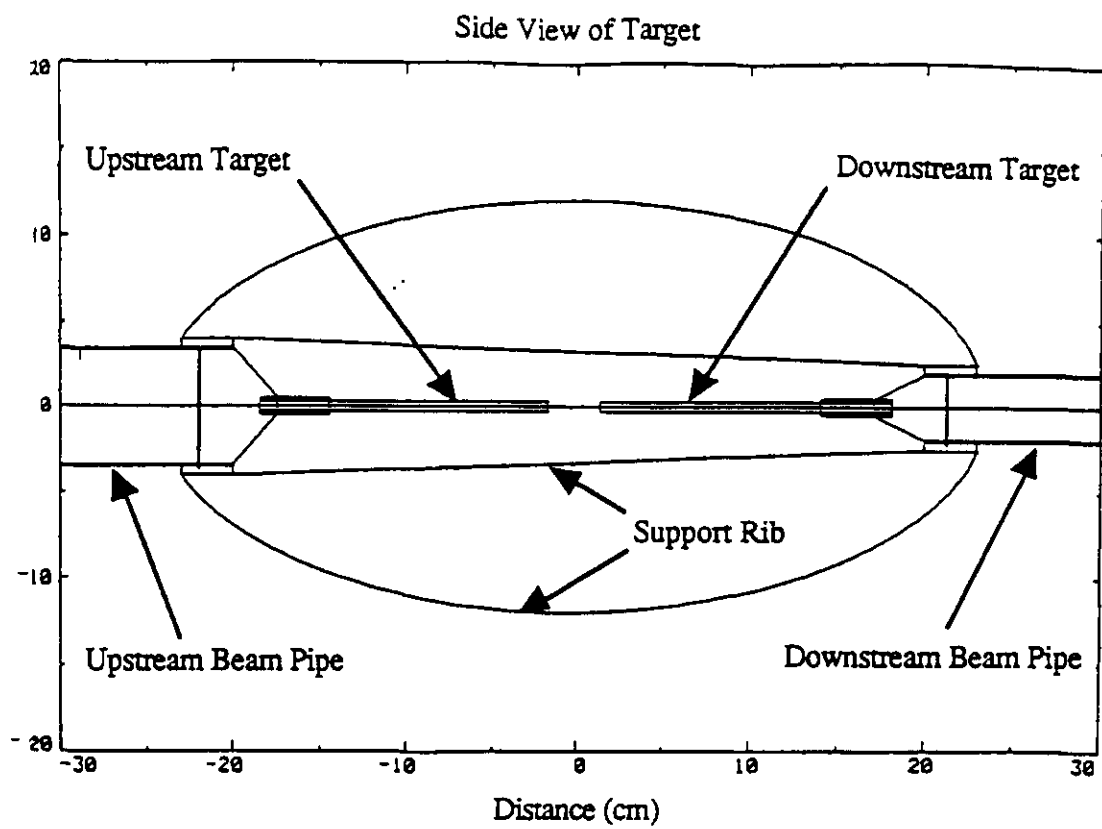


Fig. 7

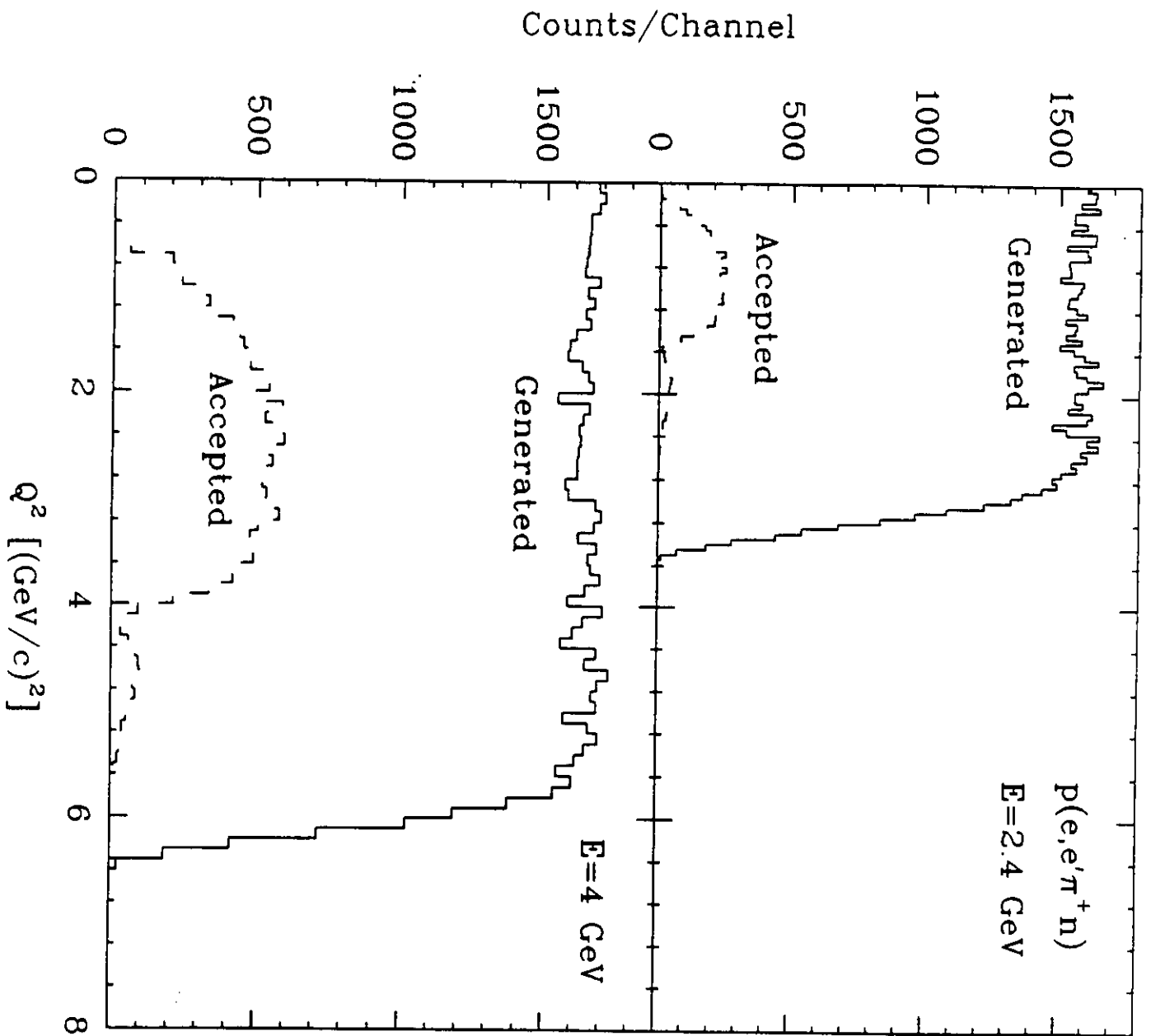


Fig. 8

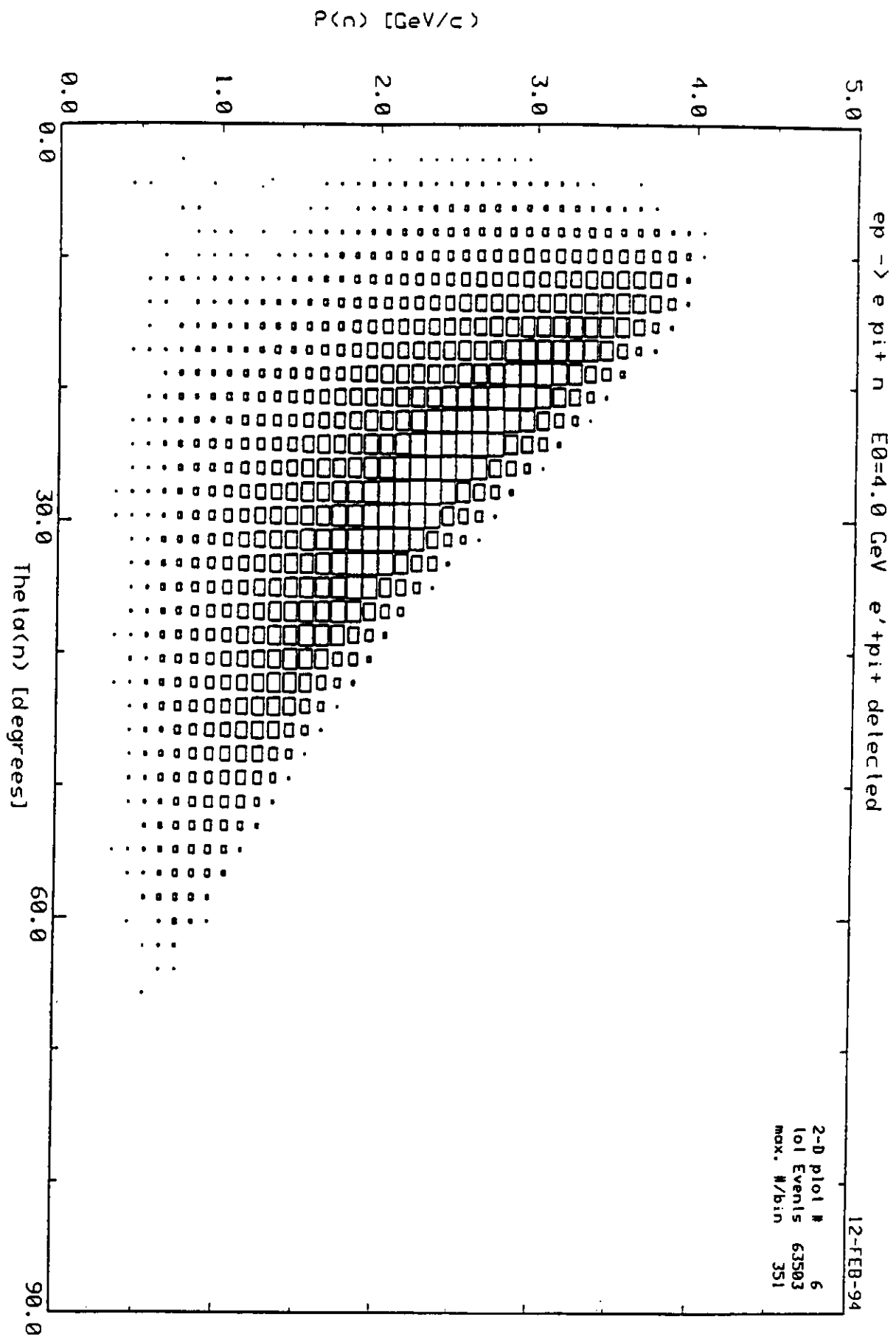


Fig. 9

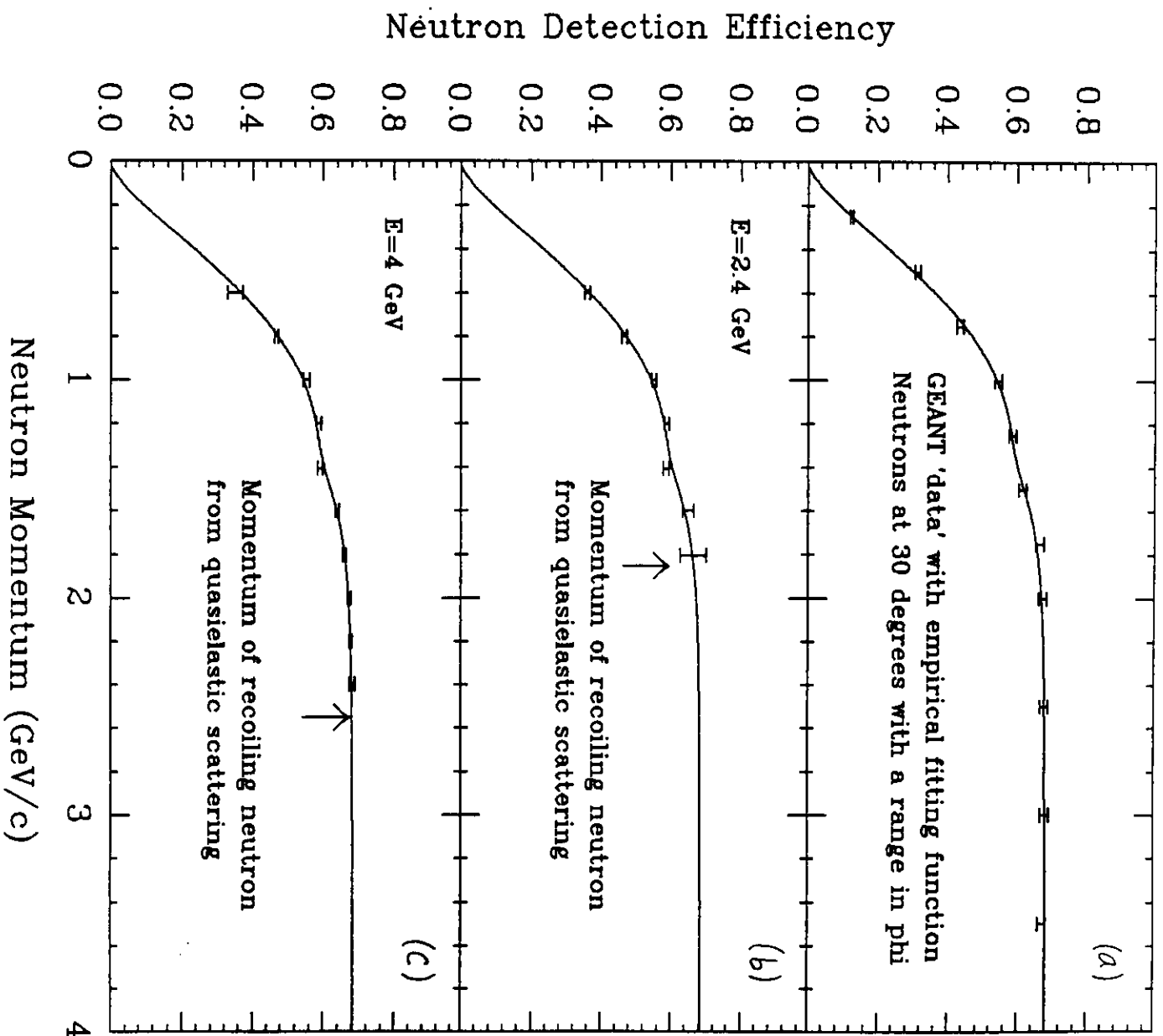


Fig. 10

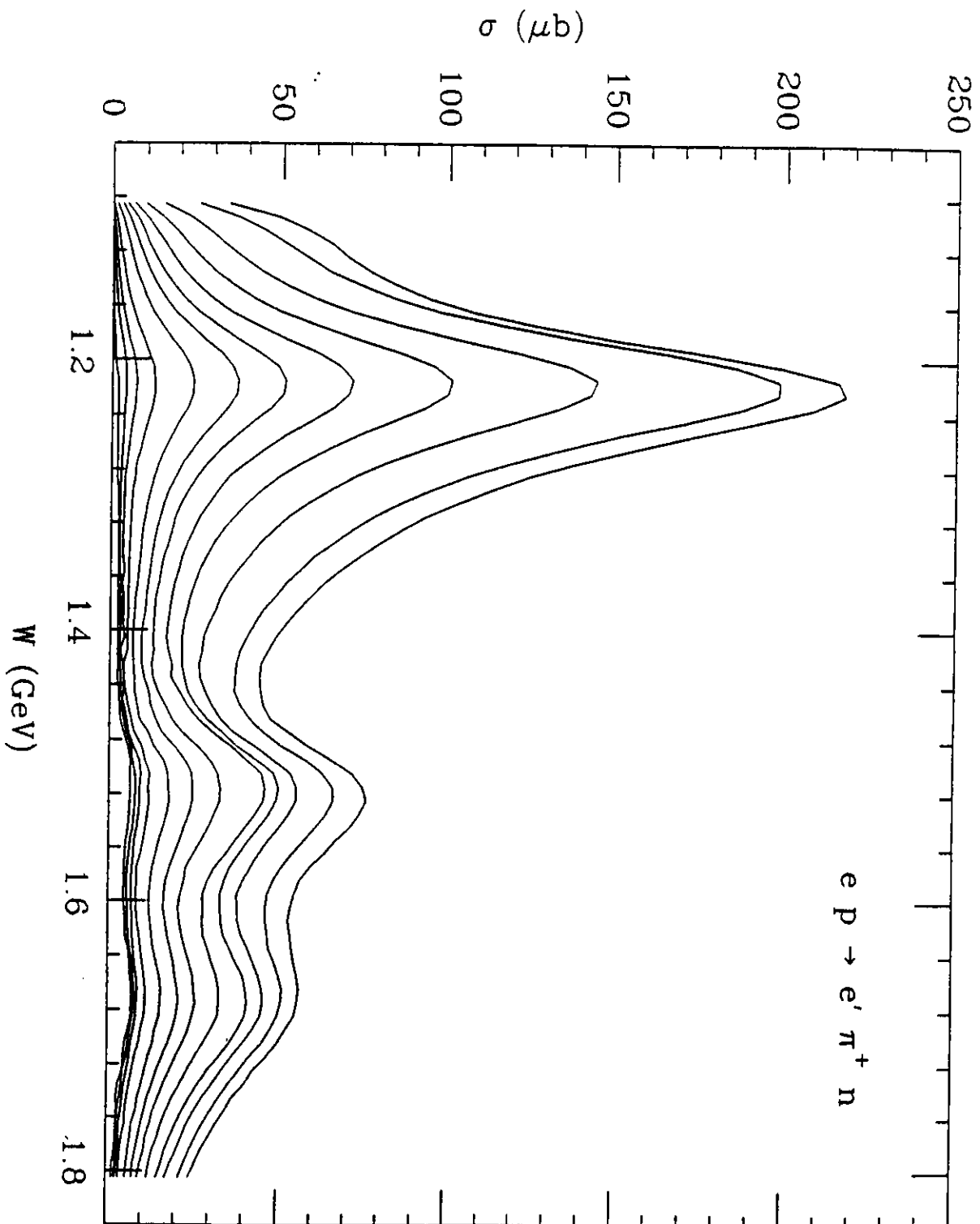


Fig. 11

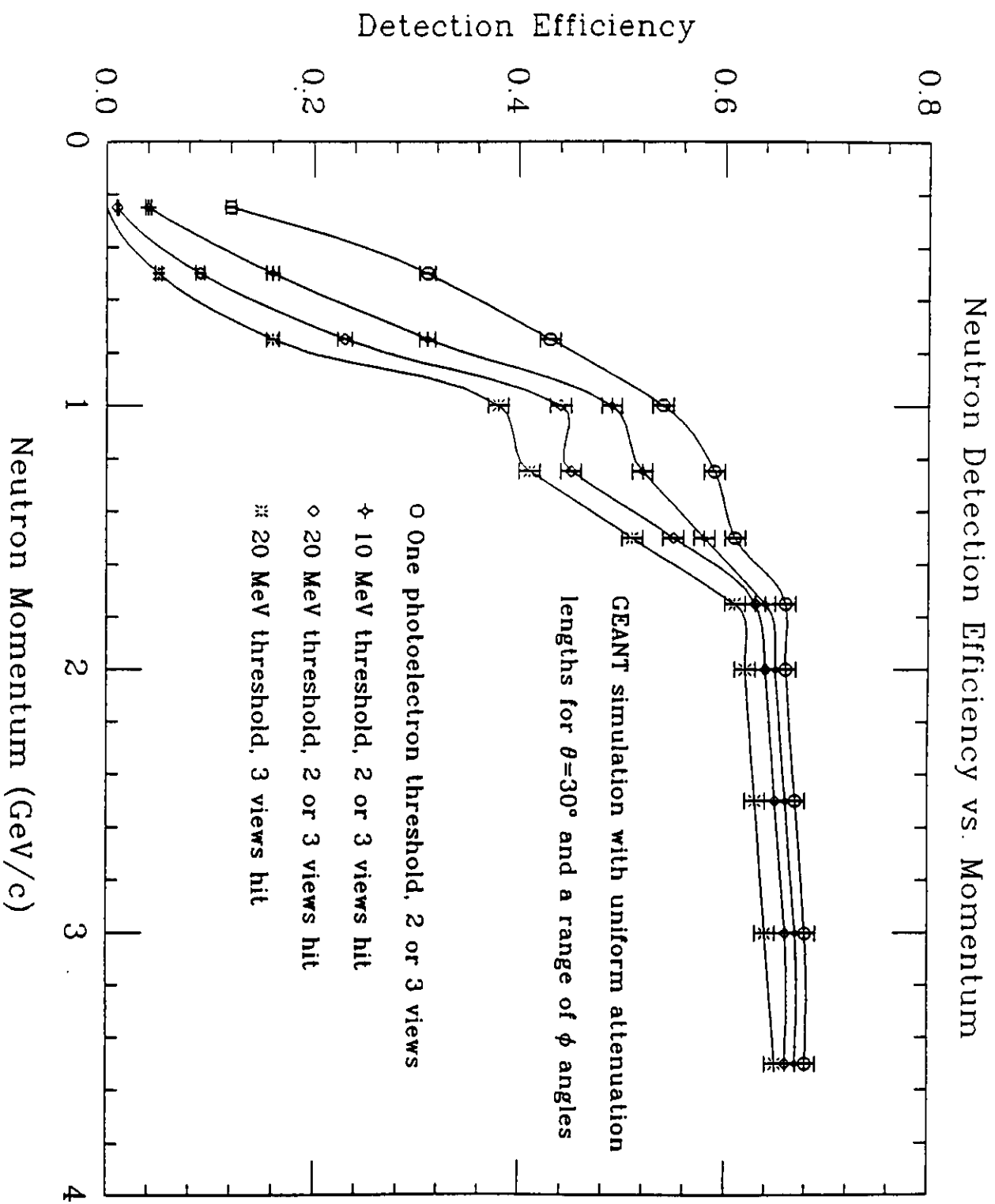
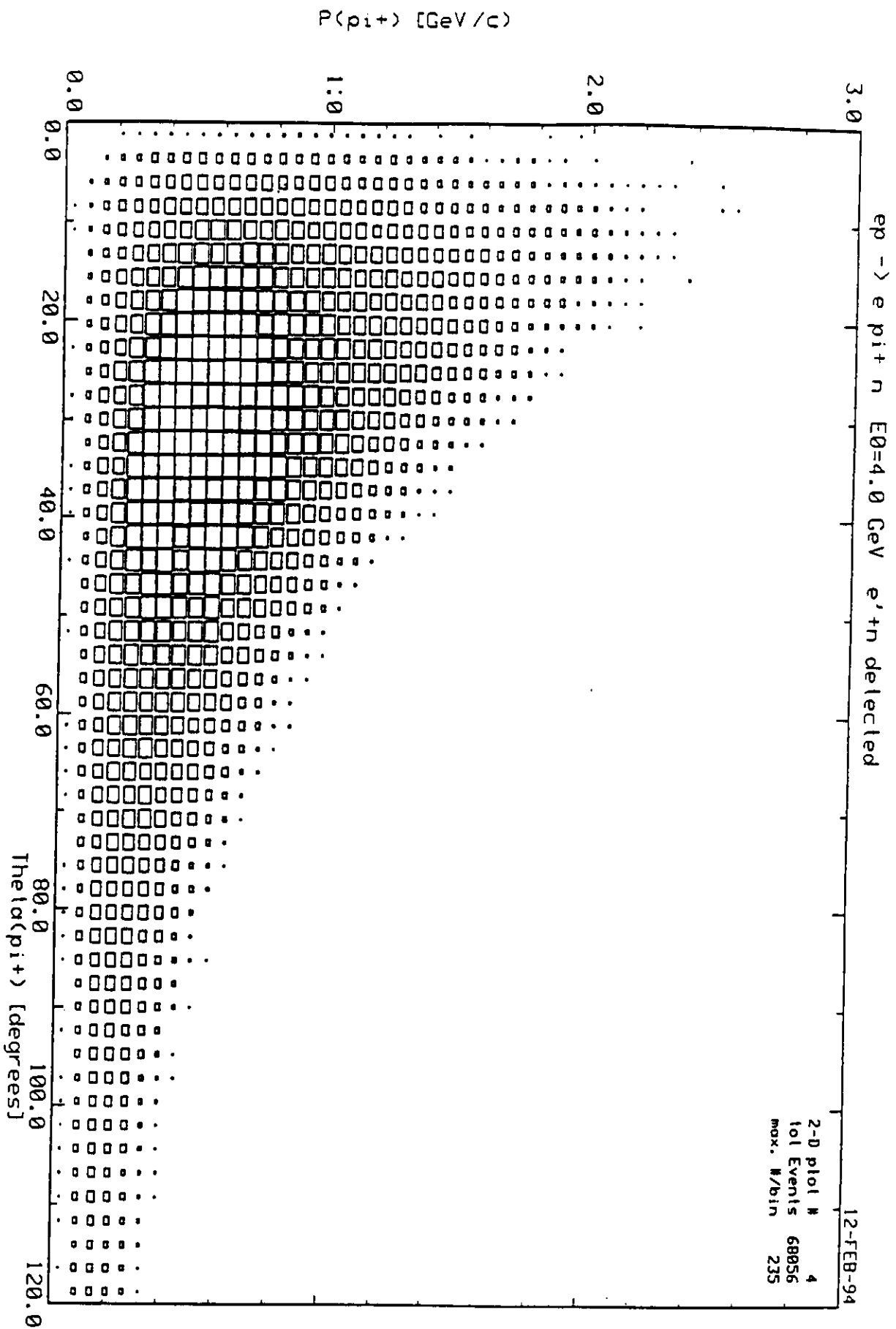


Fig. 12



Precision Cross-check of Calorimeter Geometry vs. Drift Chamber Geometry

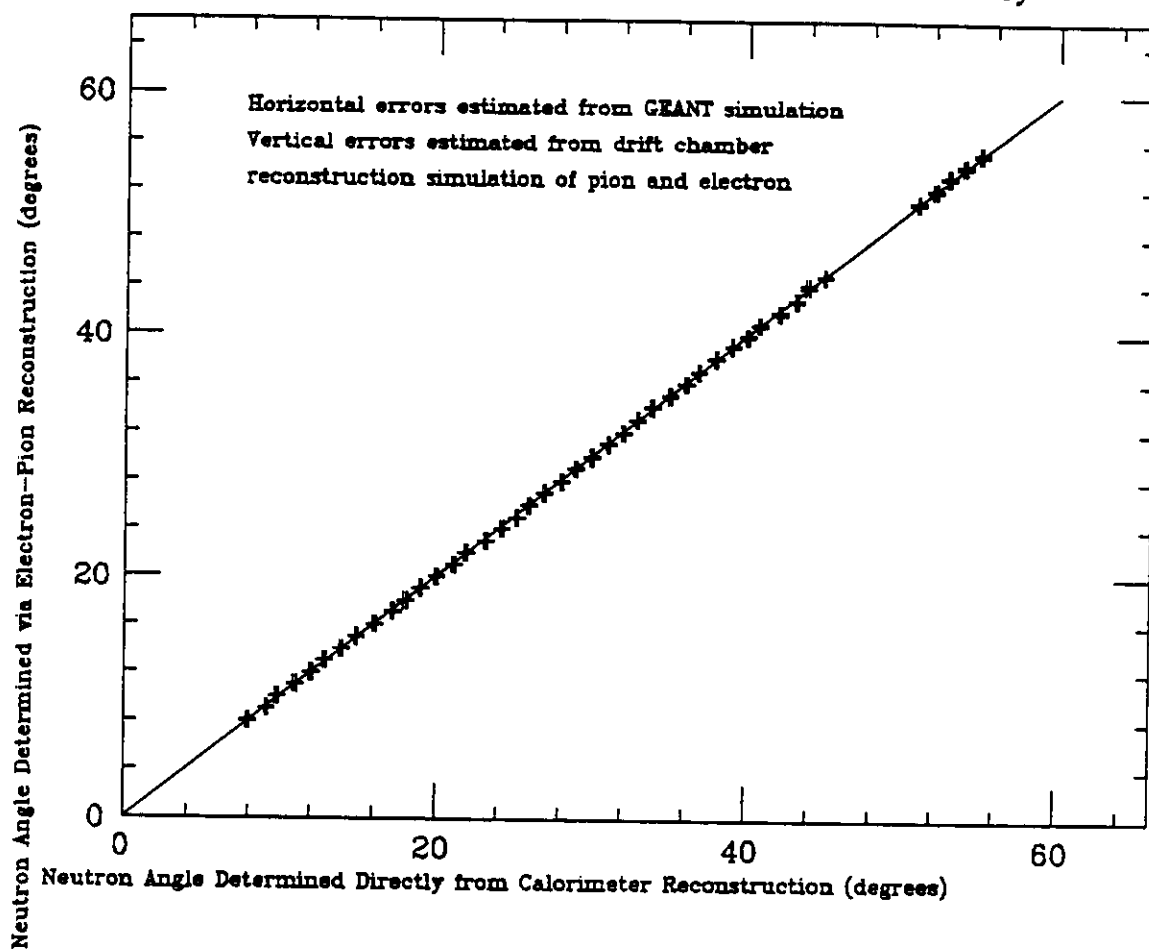


Fig. 14

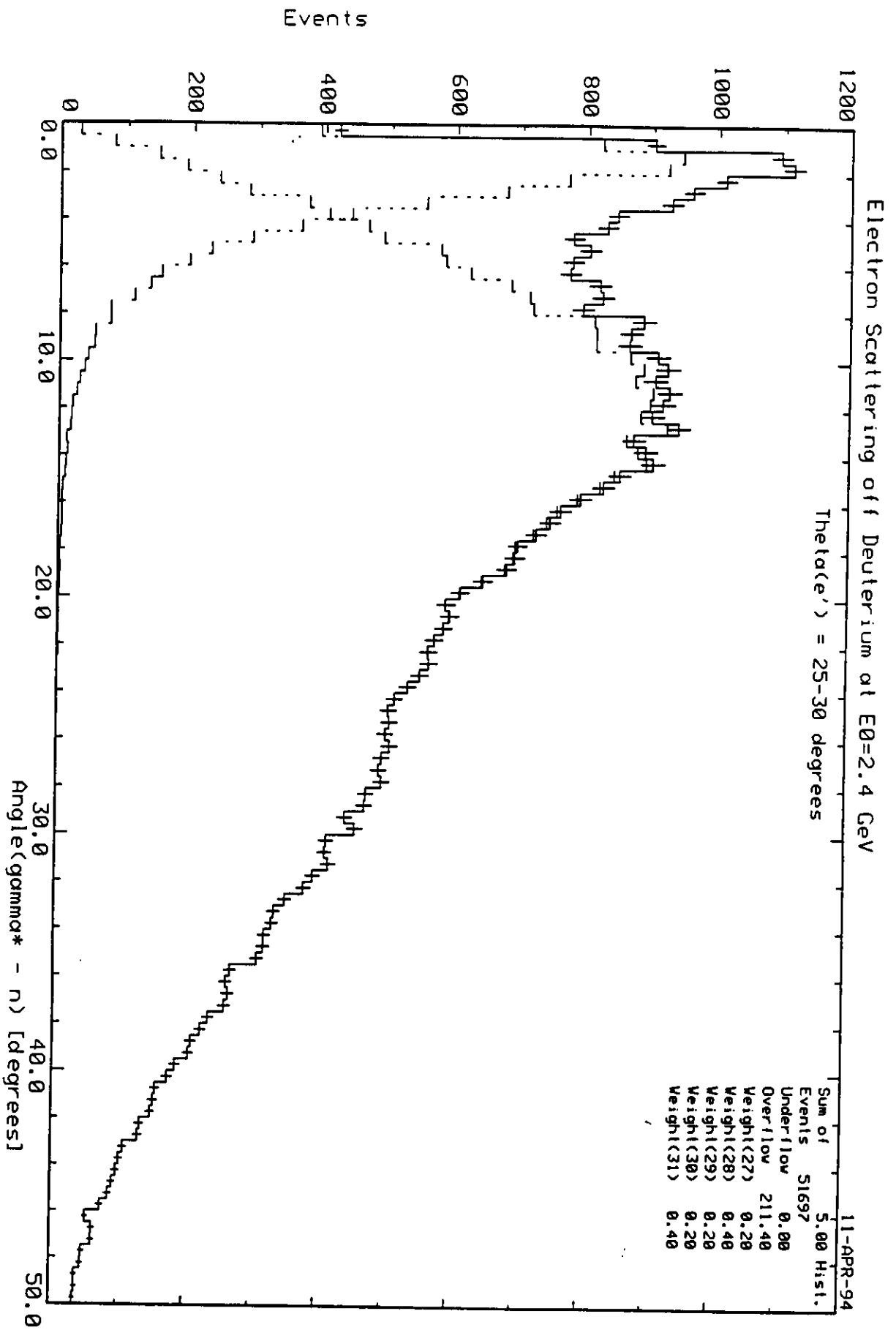


Fig. 15

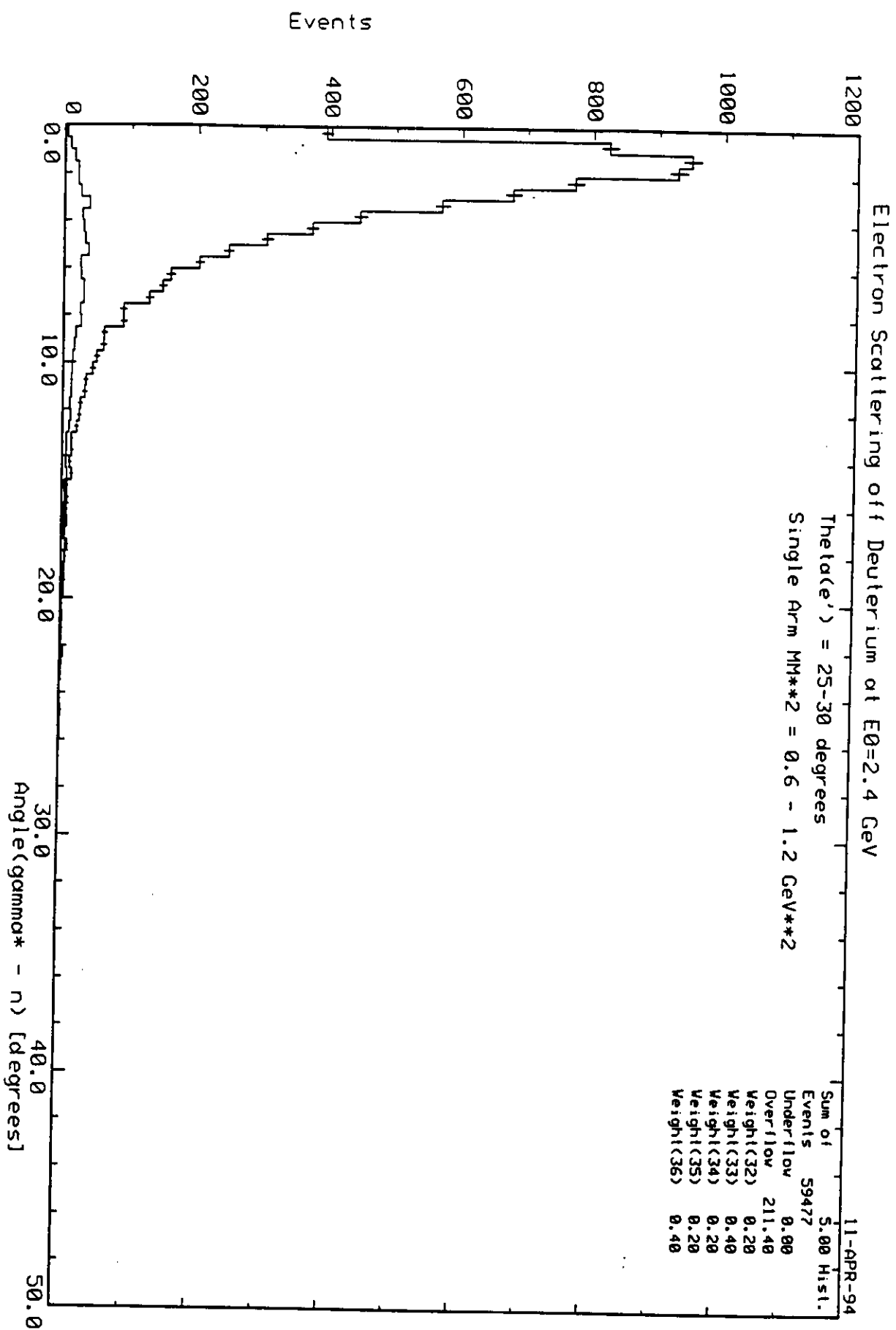


Fig. 16

Error from Neutron Angle Cut

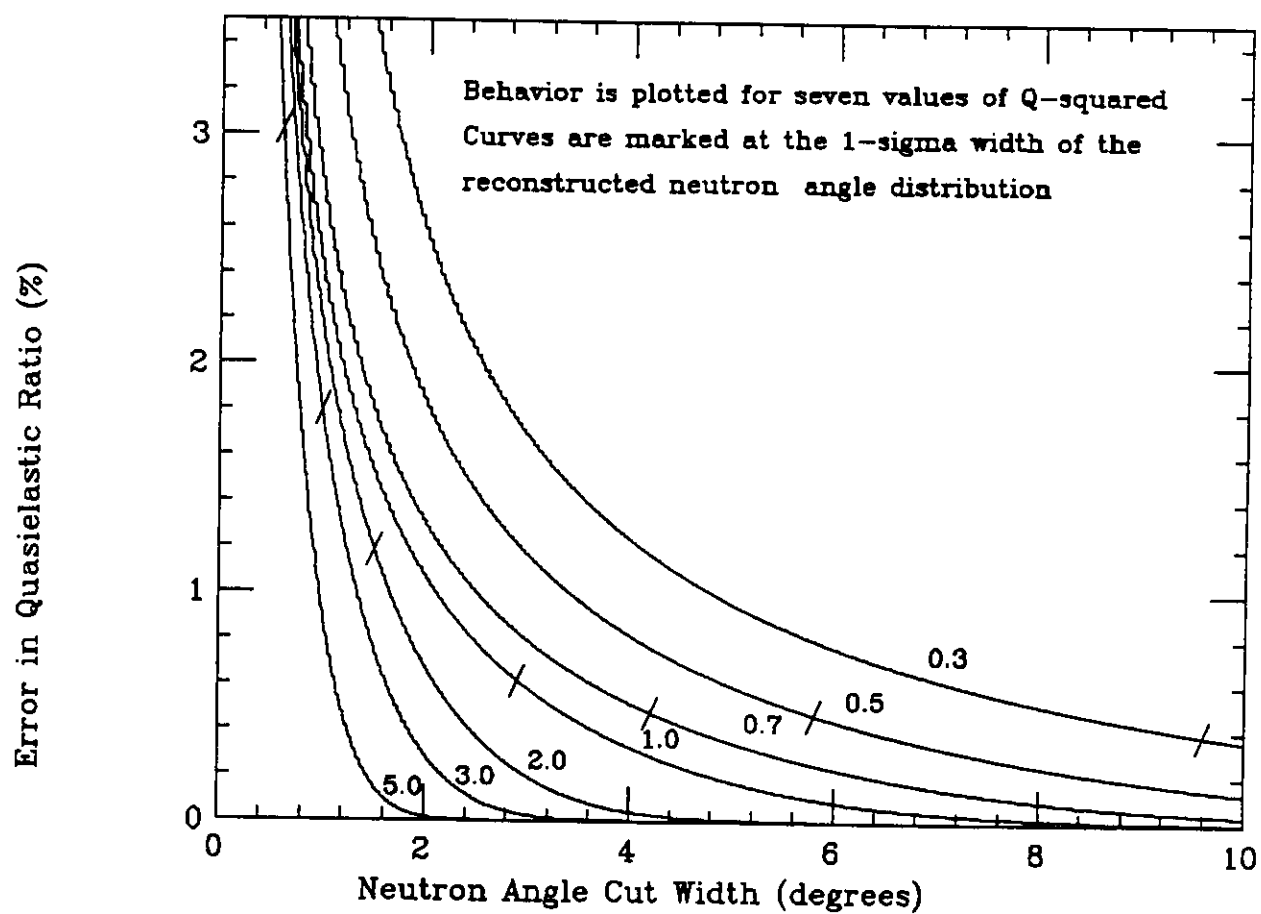


Fig. 17

Variation in Neutron Angular Resolution with Neutron Momentum

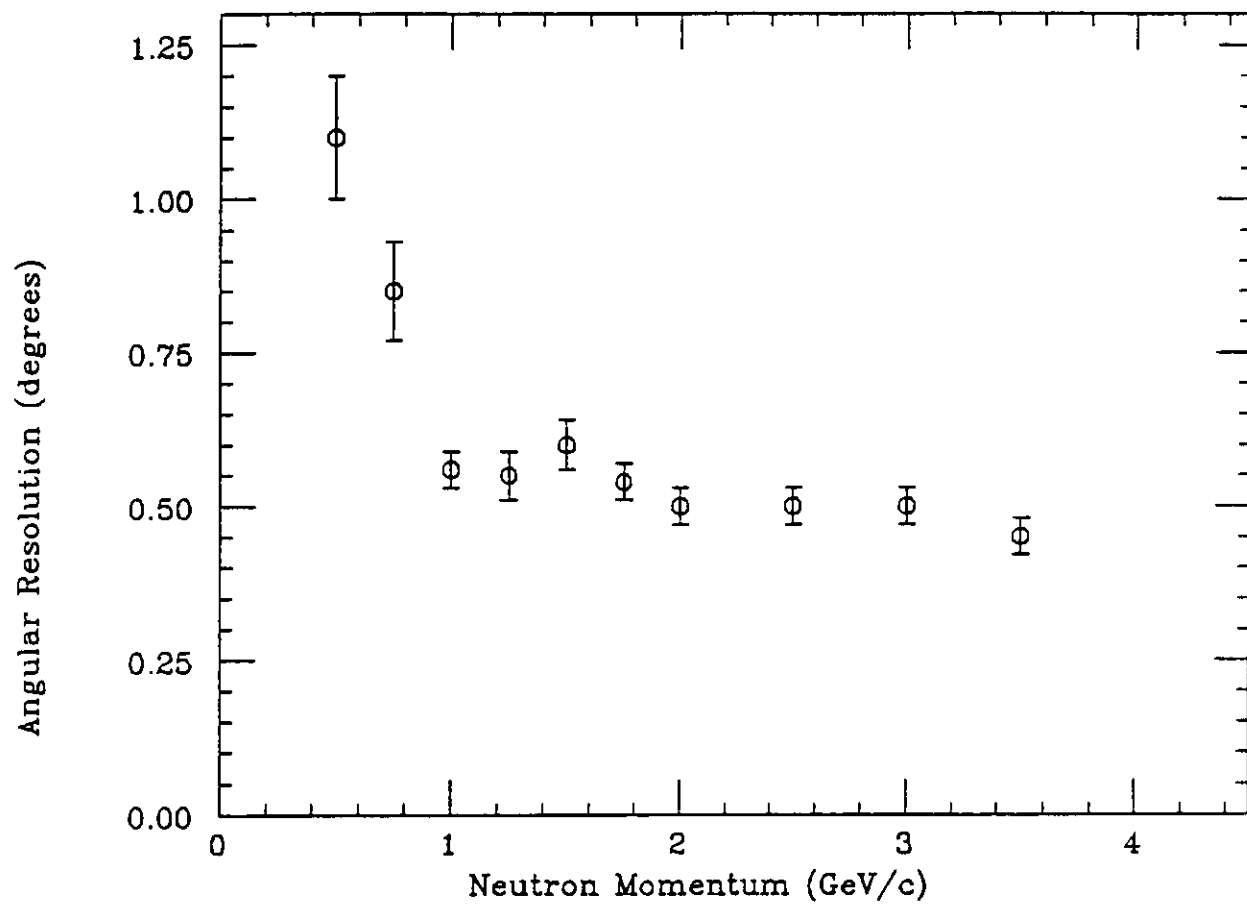


Fig. 18

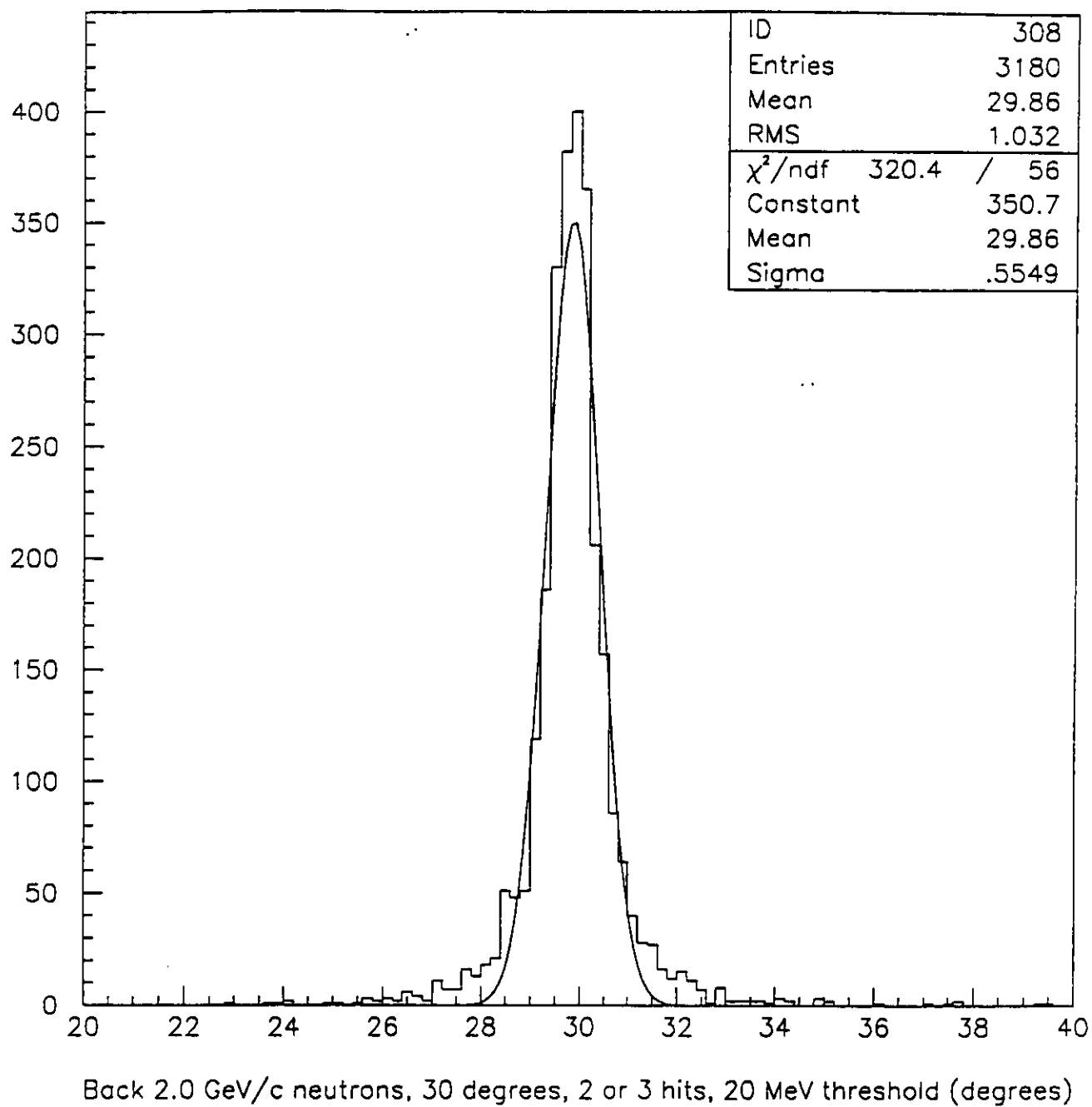


Fig. 19

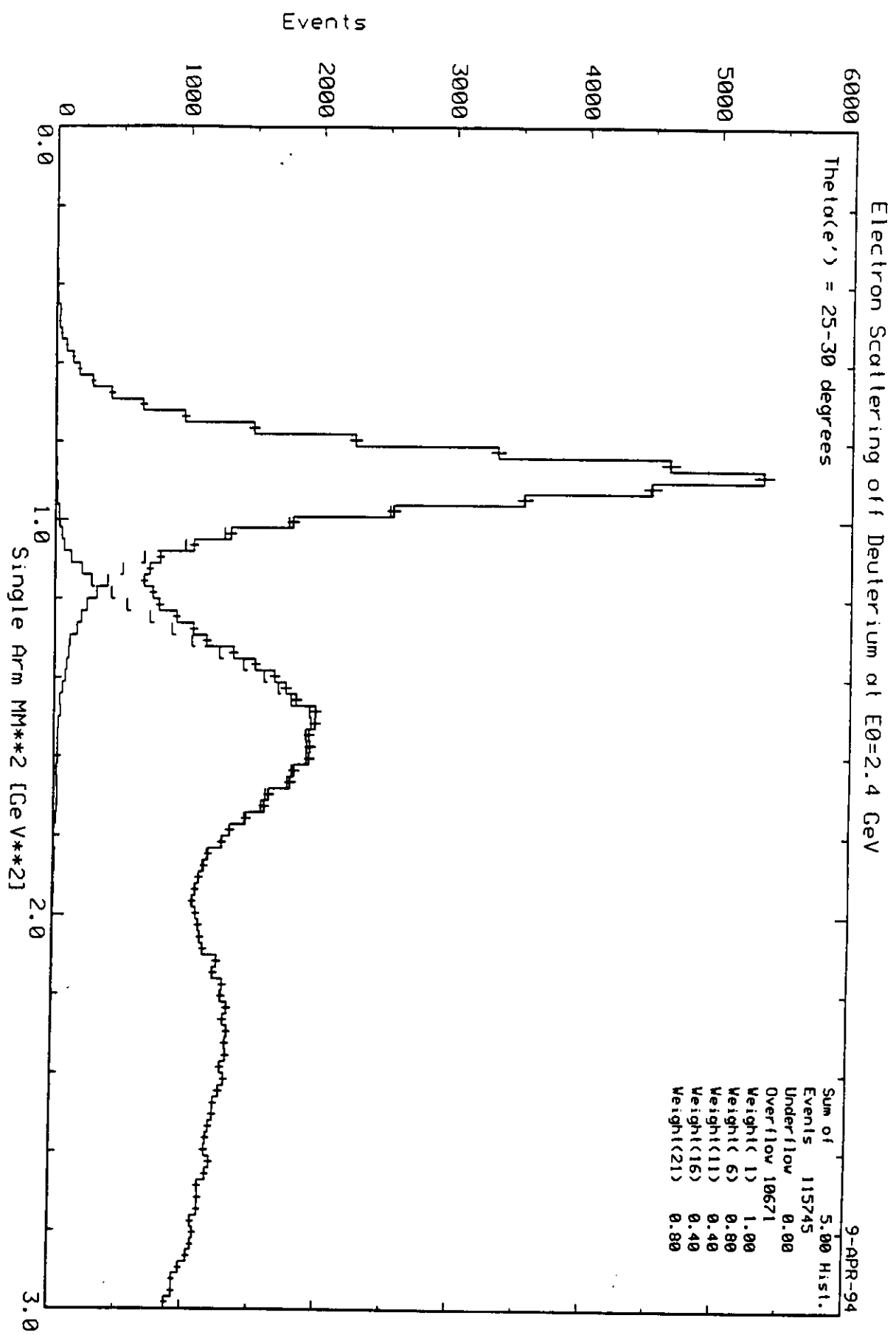


Fig. 20

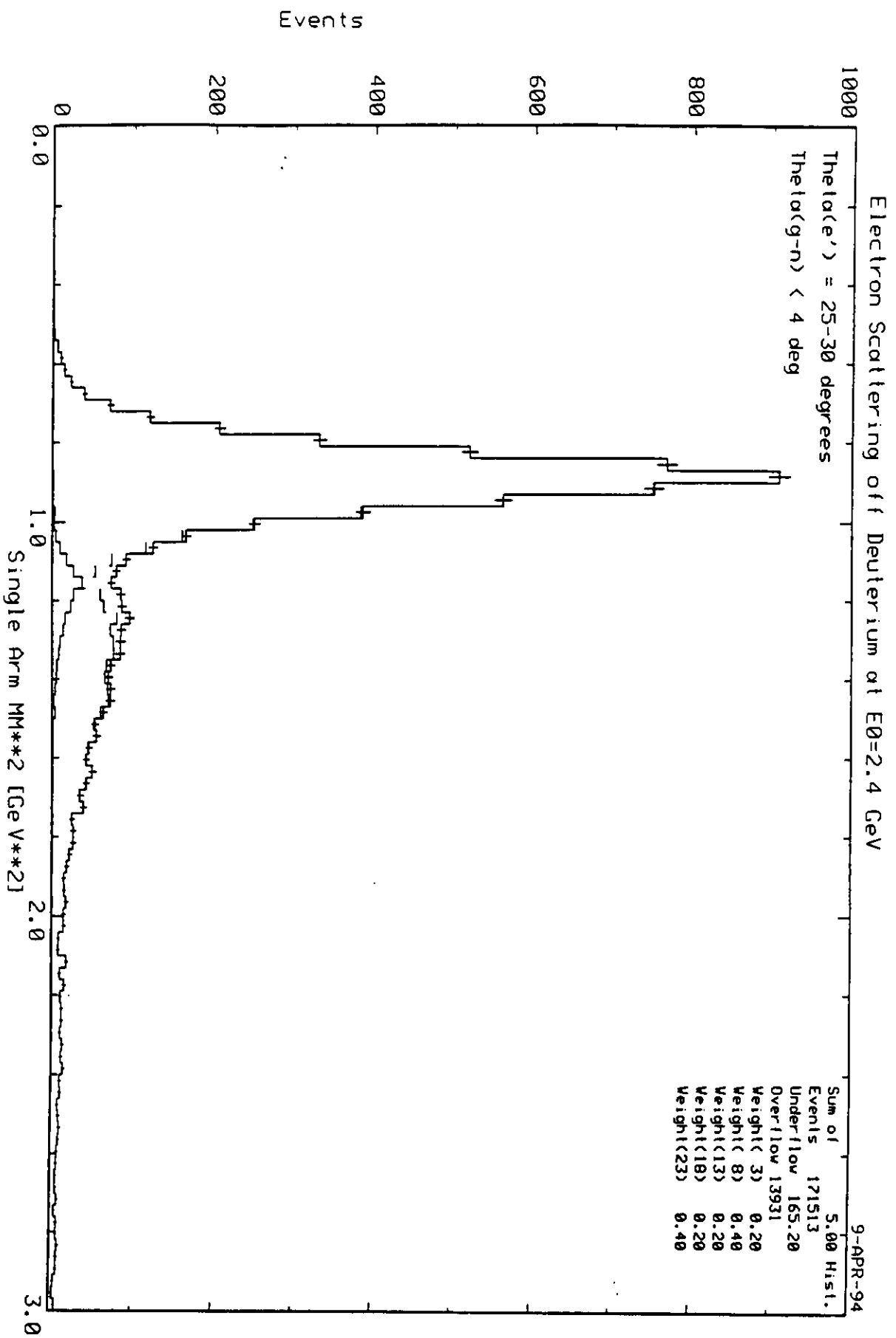


Fig. 21

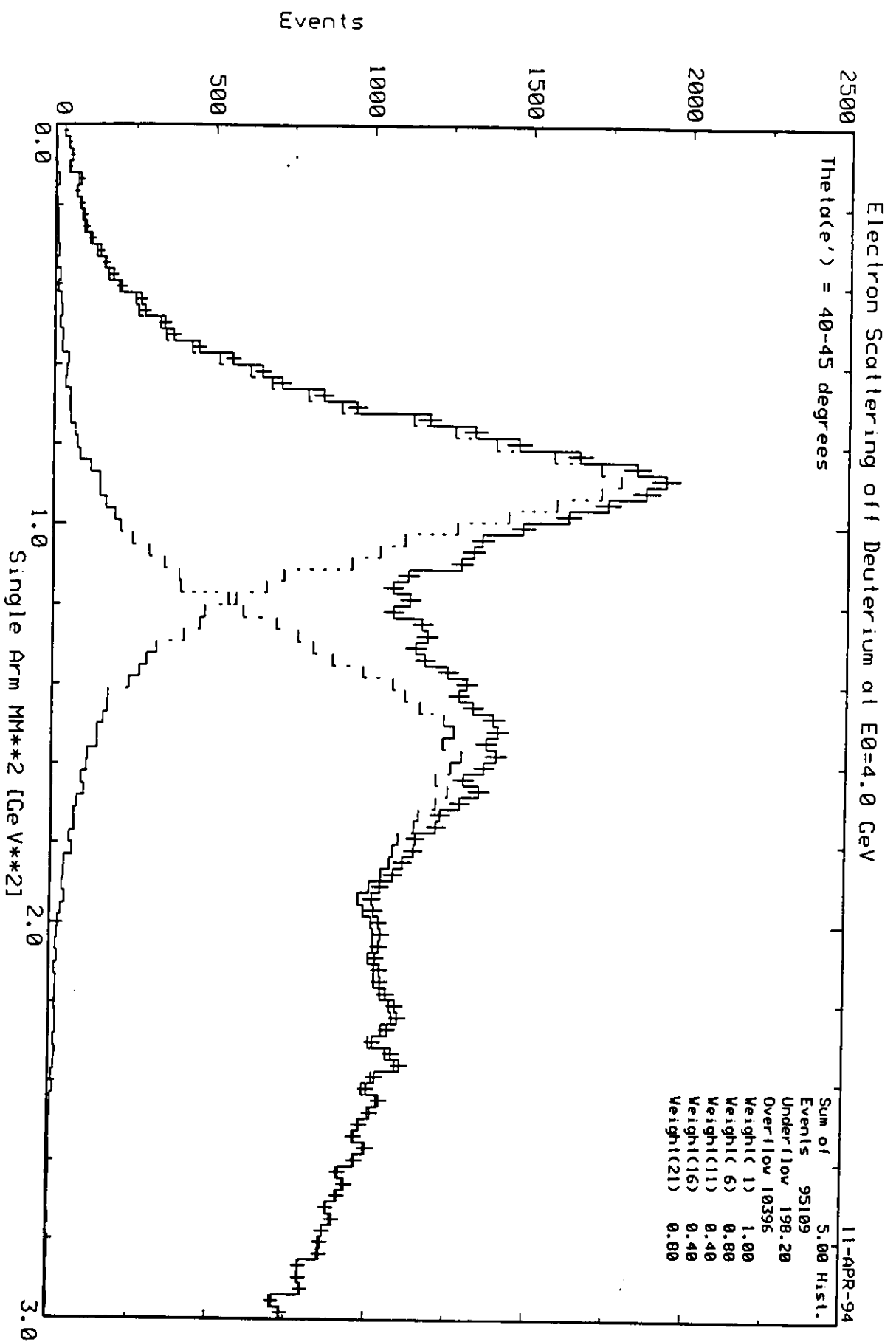


Fig. 22

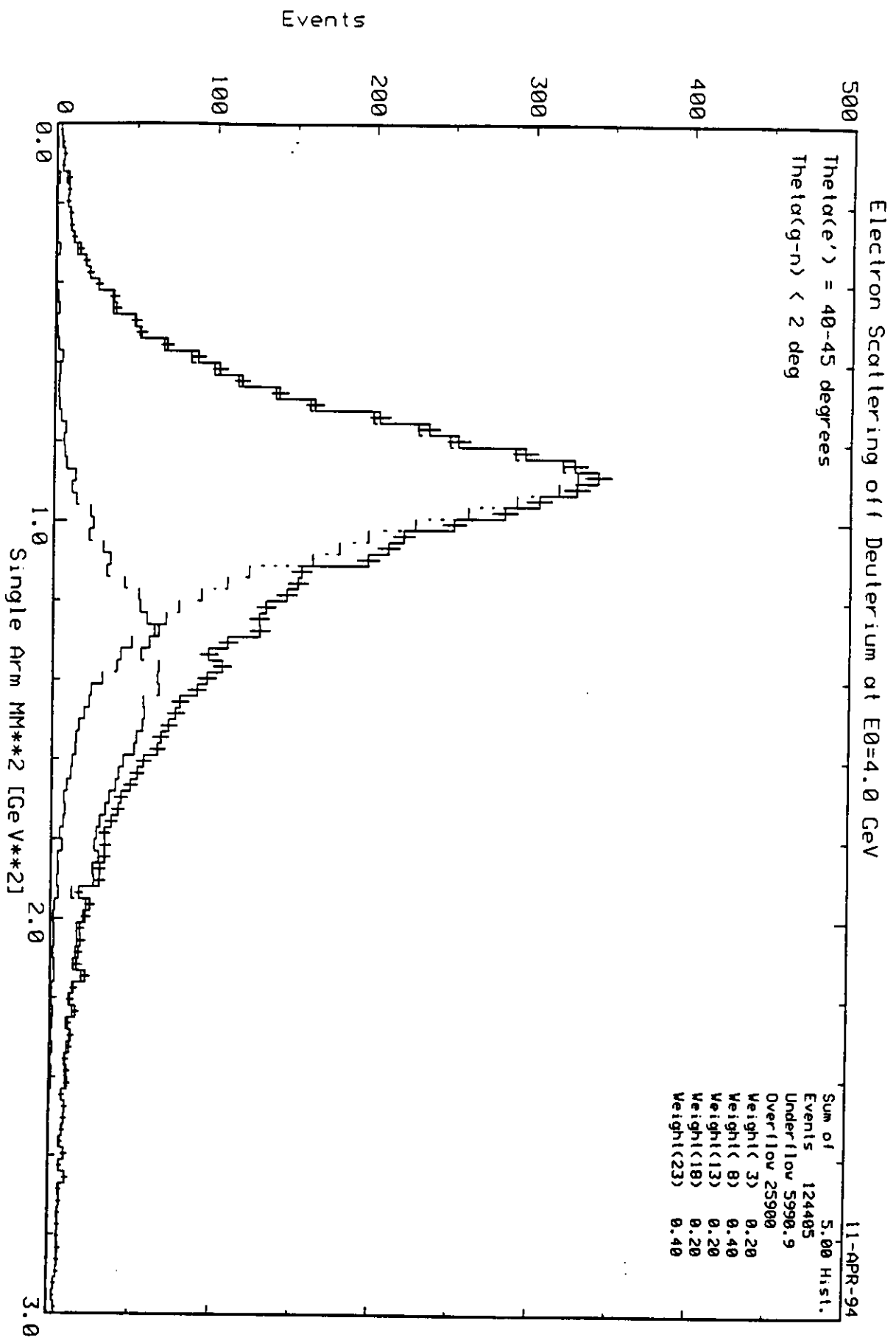


Fig. 23

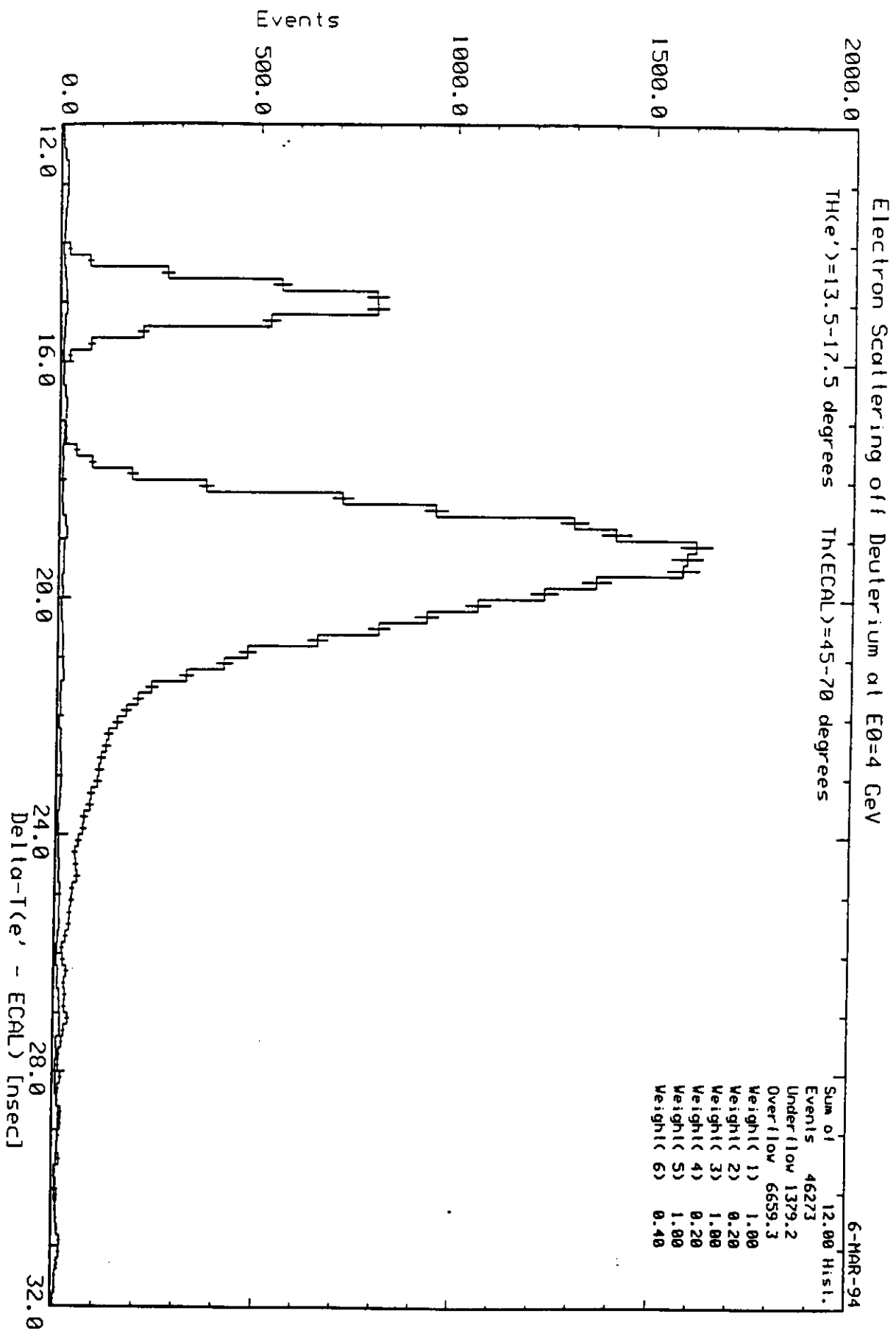


Fig. 24

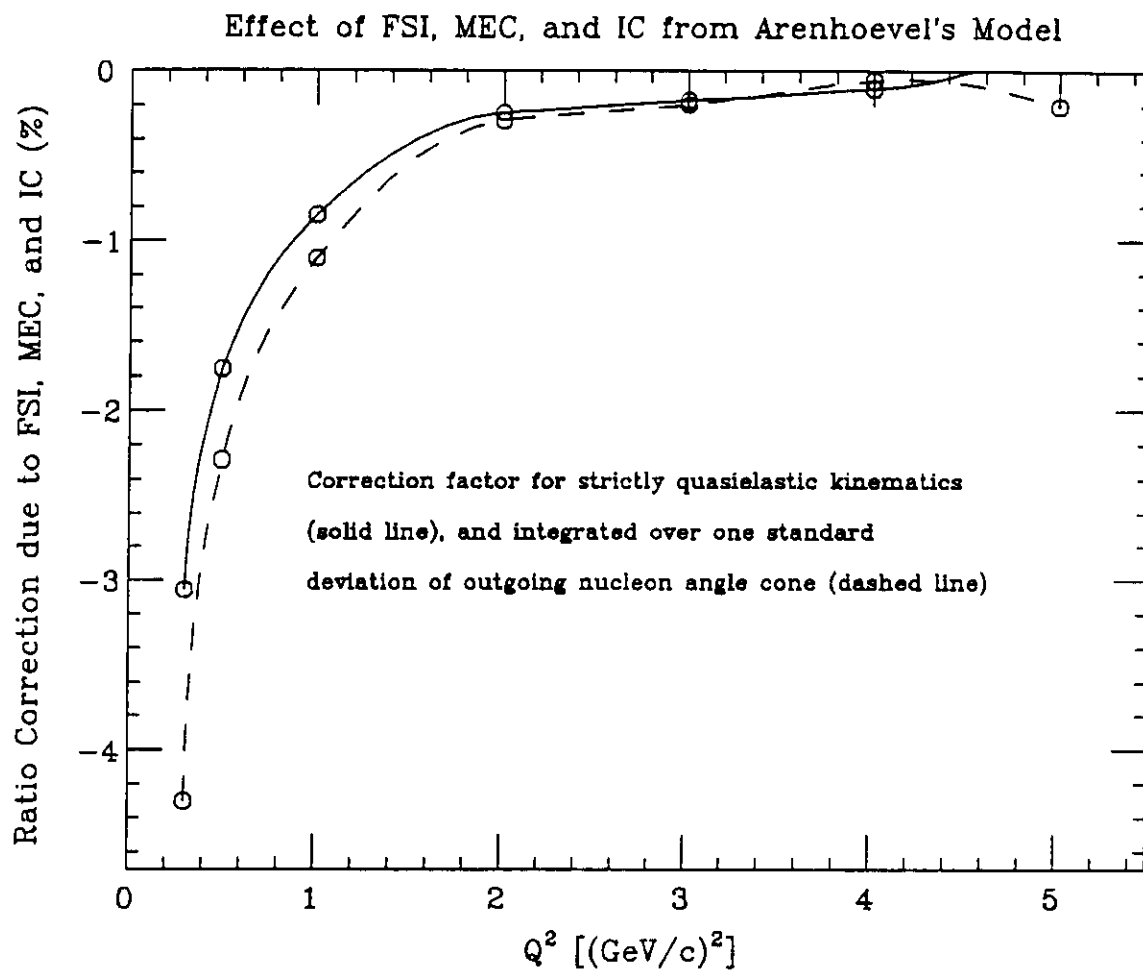


Fig. 25

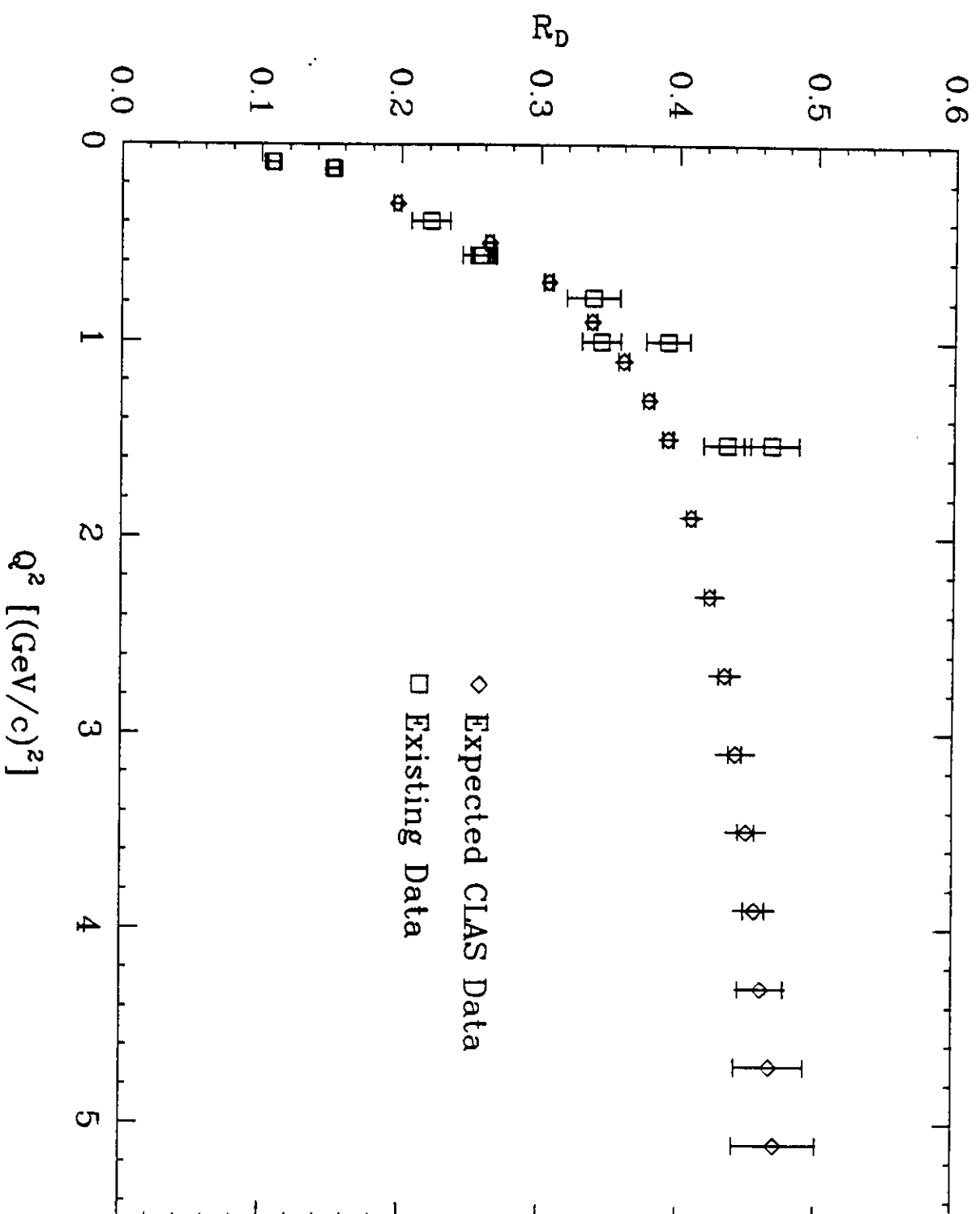


Fig. 26

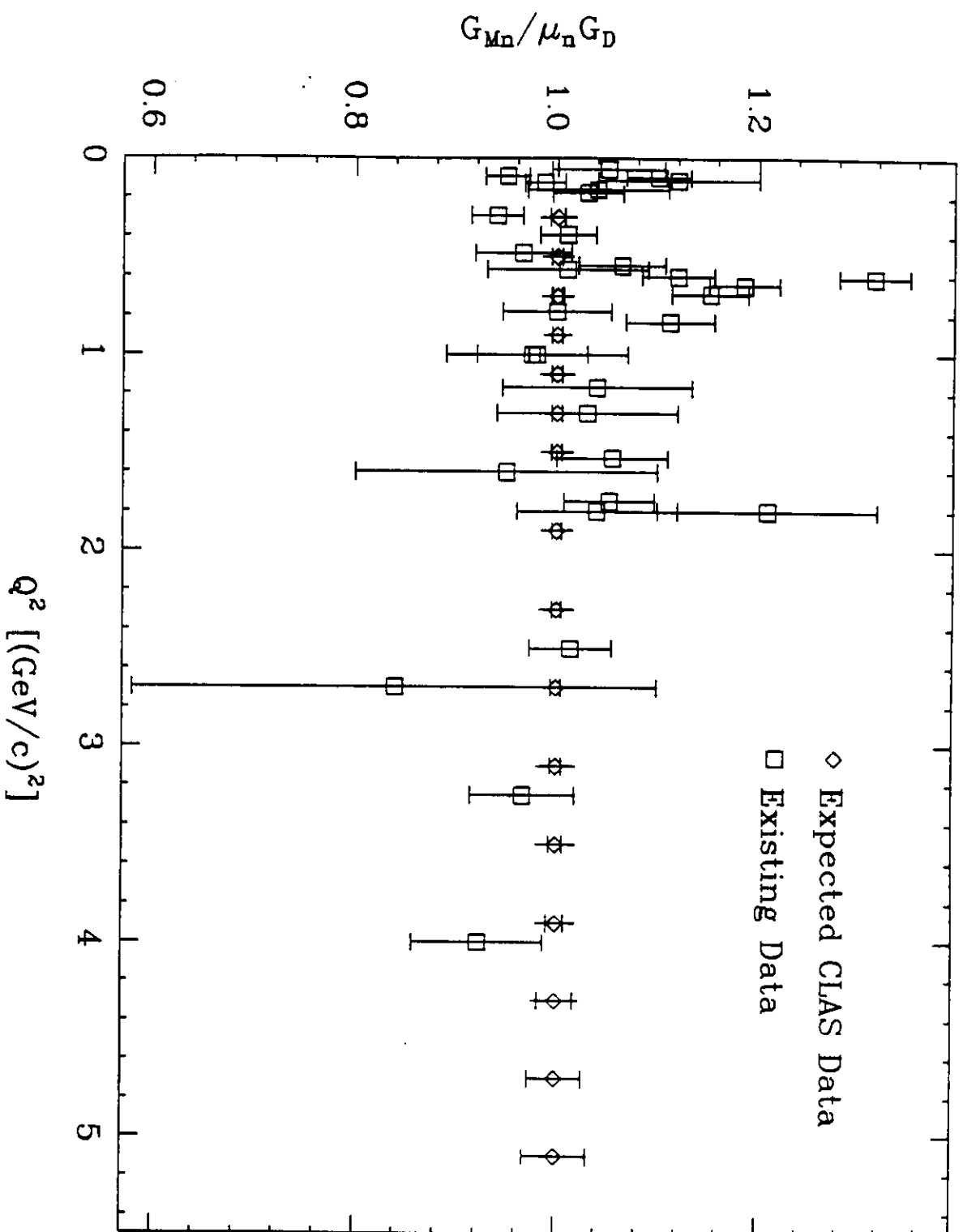


Fig. 27